Editors' Suggestion

Test of lepton flavor universality by the measurement of the $B^0 \to D^{*-}\tau^+\nu_\tau$ branching fraction using three-prong τ decays

R. Aaij *et al.*[*]
(LHCb Collaboration)

(Received 8 November 2017; published 25 April 2018)

The ratio of branching fractions $\mathcal{R}(D^{*-}) \equiv \mathcal{B}(B^0 \to D^{*-}\tau^+\nu_\tau)/\mathcal{B}(B^0 \to D^{*-}\mu^+\nu_\mu)$ is measured using a data sample of proton-proton collisions collected with the LHCb detector at center-of-mass energies of 7 and 8 TeV, corresponding to an integrated luminosity of 3 fb^{-1}. The τ lepton is reconstructed with three charged pions in the final state. A novel method is used that exploits the different vertex topologies of signal and backgrounds to isolate samples of semitauonic decays of b hadrons with high purity. Using the $B^0 \to D^{*-}\pi^+\pi^-\pi^+$ decay as the normalization channel, the ratio $\mathcal{B}(B^0 \to D^{*-}\tau^+\nu_\tau)/\mathcal{B}(B^0 \to D^{*-}\pi^+\pi^-\pi^+)$ is measured to be $1.97 \pm 0.13 \pm 0.18$, where the first uncertainty is statistical and the second systematic. An average of branching fraction measurements for the normalization channel is used to derive $\mathcal{B}(B^0 \to D^{*-}\tau^+\nu_\tau) = (1.42 \pm 0.094 \pm 0.129 \pm 0.054)\%$, where the third uncertainty is due to the limited knowledge of $\mathcal{B}(B^0 \to D^{*-}\pi^+\pi^-\pi^+)$. A test of lepton flavor universality is performed using the well-measured branching fraction $\mathcal{B}(B^0 \to D^{*-}\mu^+\nu_\mu)$ to compute $\mathcal{R}(D^{*-}) = 0.291 \pm 0.019 \pm 0.026 \pm 0.013$, where the third uncertainty originates from the uncertainties on $\mathcal{B}(B^0 \to D^{*-}\pi^+\pi^-\pi^+)$ and $\mathcal{B}(B^0 \to D^{*-}\mu^+\nu_\mu)$. This measurement is in agreement with the Standard Model prediction and with previous measurements.

DOI: 10.1103/PhysRevD.97.072013

I. INTRODUCTION

In the Standard Model (SM) of particle physics, lepton flavor universality (LFU) is an accidental symmetry broken only by the Yukawa interactions. Differences between the expected branching fraction of semileptonic decays into the three lepton families originate from the different masses of the charged leptons. Further deviations from LFU would be a signature of physics processes beyond the SM.

Measurements of the couplings of Z and W bosons to light leptons, mainly constrained by LEP and SLC experiments, are compatible with LFU. Nevertheless, a 2.8 standard deviation difference exists between the measurement of the branching fraction of the $W^+ \to \tau^+\nu_\tau$ decay with respect to those of the branching fractions of $W^+ \to \mu^+\nu_\mu$ and $W^+ \to e^+\nu_e$ decays [1].

Since uncertainties due to hadronic effects cancel to a large extent, the SM prediction for the ratios between branching fractions of semitauonic decays of B mesons relative to decays involving lighter lepton families, such as

$$\mathcal{R}(D^{(*)-}) \equiv \mathcal{B}(B^0 \to D^{(*)-}\tau^+\nu_\tau)/\mathcal{B}(B^0 \to D^{(*)-}\mu^+\nu_\mu), \quad (1)$$

$$\mathcal{R}(D^{(*)0}) \equiv \mathcal{B}(B^- \to D^{(*)0}\tau^-\bar{\nu}_\tau)/\mathcal{B}(B^- \to D^{(*)0}\mu^-\bar{\nu}_\mu), \quad (2)$$

is known with an uncertainty at the percent level [2–5]. For D^* decays, recent papers [5,6] argue for larger uncertainties, up to 4%. These decays therefore provide a sensitive probe of SM extensions with flavor-dependent couplings, such as models with an extended Higgs sector [7], with leptoquarks [8,9], or with an extended gauge sector [10–12].

The $B \to D^{(*)}\tau^+\nu_\tau$ decays have recently been subject to intense experimental scrutiny. Measurements of $\mathcal{R}(D^{0,-})$ and $\mathcal{R}(D^{*-,0})$ and their averages $\mathcal{R}(D)$ and $\mathcal{R}(D^*)$ have been reported by the *BABAR* [13,14] and Belle [15,16] Collaborations in final states involving electrons or muons from the τ decay. The LHCb Collaboration measured $\mathcal{R}(D^*)$ [17] with results compatible with those from *BABAR*, while the result from the Belle Collaboration is compatible with the SM within 1 standard deviation. The measurements from both the *BABAR* and Belle Collaborations were performed with events that were "tagged" by fully reconstructing the decay of one of the two B mesons from the $\Upsilon(4S)$ decay to a fully hadronic final state (hadronic tag); the other B meson was used to search for the signal. In all of the above measurements, the decay of the τ lepton into a muon, or an electron, and two neutrinos was exploited. More recently, the Belle Collaboration published a measurement [16] with

[*]Full author list given at the end of the article.

events tagged using semileptonic decays, compatible with the SM within 1.6 standard deviations. A simultaneous measurement of $\mathcal{R}(D^*)$ and of the τ polarization, using hadronic tagging and reconstruction of the $\tau^- \to \pi^-\nu_\tau$ and $\tau^- \to \rho^-\nu_\tau$ decays, was published by the Belle Collaboration [18,19]. The average of all these $\mathcal{R}(D^*)$ measurements is in tension with the SM expectation at 3.3 standard deviations. All these $\mathcal{R}(D^{(*)-,0})$ measurements yield values that are above the SM predictions with a combined significance of 3.9 standard deviations [20].

This paper presents a measurement of $\mathcal{B}(B^0 \to D^{*-}\tau^+\nu_\tau)$, using for the first time the τ decay with three charged particles (three-prong) in the final state, i.e. $\tau^+ \to \pi^+\pi^-\pi^+\bar{\nu}_\tau$ and $\tau^+ \to \pi^+\pi^-\pi^+\pi^0\bar{\nu}_\tau$, denoted as *signal* in this paper. The D^{*-} meson is reconstructed through the $D^{*-} \to \bar{D}^0(\to K^+\pi^-)\pi^-$ decay chain.[1] The visible final state consists of six charged tracks; neutral pions are not reconstructed in this analysis. A data sample of proton-proton collisions, corresponding to an integrated luminosity of 3 fb^{-1}, collected with the LHCb detector at center-of-mass energies of $\sqrt{s} = 7$ and 8 TeV is used. A shorter version of this paper can be found in Ref. [21]

The three-prong τ decay modes have different features with respect to leptonic τ decays, leading to measurements with a better signal-to-background ratio and statistical significance. The absence of charged leptons in the final state avoids backgrounds originating from semileptonic decays of b or c hadrons. The three-prong topology enables the precise reconstruction of a τ decay vertex detached from the B^0 decay vertex due to the nonzero τ lifetime, thereby allowing the discrimination between signal decays and the most abundant background due to $B \to D^{*-}3\pi X$ decays, where X represents unreconstructed particles and $3\pi \equiv \pi^+\pi^-\pi^+$.[2] The requirement of a 3π decay vertex detached from the B vertex suppresses the $D^{*-}3\pi X$ background by three orders of magnitude, while retaining about 40% of the signal. Moreover, because only one neutrino is produced in the τ decay, the measurements of the B^0 and τ lines of flight allow the determination of the complete kinematics of the decay, up to two quadratic ambiguities, leading to four solutions.

After applying the 3π detached-vertex requirement, the dominant background consists of B decays with a D^{*-} and another charm hadron in the final state, called *double-charm* hereafter. The largest component is due to $B \to D^{*-}D_s^+(X)$ decays. These decays have the same topology as the signal, as the second charm hadron has a measurable lifetime and its decay vertex is detached from the B vertex. The double-charm background is suppressed by applying vetoes on the presence of additional particles around the direction of the τ and B candidates, and exploiting the different resonant structure of the 3π system in τ^+ and D_s^+ decays.

The signal yield, $N_{\rm sig}$, is normalized to that of the exclusive $B^0 \to D^{*-}3\pi$ decay, $N_{\rm norm}$, which has the same charged particles in the final state. This choice minimizes experimental systematic uncertainties. The measured quantity is

$$\mathcal{K}(D^{*-}) \equiv \frac{\mathcal{B}(B^0 \to D^{*-}\tau^+\nu_\tau)}{\mathcal{B}(B^0 \to D^{*-}3\pi)} = \frac{N_{\rm sig}}{N_{\rm norm}}\frac{\varepsilon_{\rm norm}}{\varepsilon_{\rm sig}}\frac{1}{\mathcal{B}(\tau^+ \to 3\pi\bar{\nu}_\tau) + \mathcal{B}(\tau^+ \to 3\pi\pi^0\bar{\nu}_\tau)}, \quad (3)$$

where $\varepsilon_{\rm sig}$ and $\varepsilon_{\rm norm}$ are the efficiencies for the signal and normalization decay modes, respectively. More precisely, $\varepsilon_{\rm sig}$ is the weighted average efficiency for the 3π and the 3π π^0 modes, given their respective branching fractions. The absolute branching fraction is obtained as $\mathcal{B}(B^0 \to D^{*-}\tau^+\nu_\tau) = \mathcal{K}(D^{*-}) \times \mathcal{B}(B^0 \to D^{*-}3\pi)$, where the branching fraction of the $B^0 \to D^{*-}3\pi$ decay is taken by averaging the measurements of Refs. [22–24]. A value for $\mathcal{R}(D^{*-})$ is then derived by using the branching fraction of the $B^0 \to D^{*-}\mu^+\nu_\mu$ decay from Ref. [20].

This paper is structured as follows. Descriptions of the LHCb detector, the data and simulation samples and the trigger selection criteria are given in Sec. II. Signal selection and background suppression strategies are summarized in Sec. III. Section IV presents the study performed to characterize double-charm backgrounds due to $B \to D^{*-}D_s^+(X)$, $B \to D^{*-}D^+(X)$ and $B \to D^{*-}D^0(X)$ decays. The strategy used to fit the signal yield and the corresponding results are presented in Sec. V. The determination of the yield of the normalization mode is discussed in Sec. VI. The determination of $\mathcal{K}(D^{*-})$ is presented in Sec. VII and systematic uncertainties are discussed in Sec. VIII. Finally, overall results and conclusions are given in Sec. IX.

II. DETECTOR AND SIMULATION

The LHCb detector [25,26] is a single-arm forward spectrometer covering the pseudorapidity range $2 < \eta < 5$, designed for the study of particles containing b or c quarks. The detector includes a high-precision tracking system consisting of a silicon-strip vertex detector surrounding the pp interaction region [27], a large-area silicon-strip detector located upstream of a dipole magnet with a bending power of about 4 Tm, and three stations of silicon-strip detectors and straw drift tubes [28] placed downstream of the magnet. The tracking system provides a measurement of momentum, p, of charged particles with a relative uncertainty that varies from 0.5% at low momentum to 1.0% at 200 GeV/c. The minimum distance of a track to a

[1]The inclusion of charge-conjugate decay modes is implied in this paper.

[2]The notation X is used when unreconstructed particles are known to be present in the decay chain and (X) when unreconstructed particles may be present in the decay chain.

primary vertex (PV), the impact parameter (IP), is measured with a resolution of $(15 + 29/p_{\mathrm{T}})$ μm, where p_{T} is the component of the momentum transverse to the beam, in GeV/c. Different types of charged hadrons are distinguished using information from two ring-imaging Cherenkov detectors [29]. Photons, electrons and hadrons are identified by a calorimeter system consisting of scintillating-pad and preshower detectors, an electromagnetic calorimeter and a hadronic calorimeter. Muons are identified by a system composed of alternating layers of iron and multiwire proportional chambers [30].

Simulated samples of pp collisions are generated using PYTHIA [31] with a specific LHCb configuration [32]. Decays of hadronic particles are described by EvtGen [33], in which final-state radiation is generated using PHOTOS [34]. The TAUOLA package [35] is used to simulate the decays of the τ lepton into the $3\pi\,\bar{\nu}_\tau$ and $3\pi\,\pi^0\,\bar{\nu}_\tau$ final states according to the resonance chiral Lagrangian model [36] with a tuning based on the results from the *BABAR* Collaboration [37]. The interaction of the generated particles with the detector, and its response, are implemented using the GEANT4 toolkit [38] as described in Ref. [39]. The signal decays are simulated using form factors that are derived from heavy-quark effective theory [40]. The experimental values of the corresponding parameters are taken from Ref. [20], except for an unmeasured helicity-suppressed amplitude, which is taken from Ref. [41].

The trigger [42] consists of a hardware stage, based on information from the calorimeter and muon systems, followed by a software stage, in which all charged particles with $p_{\mathrm{T}} > 500(300)$ MeV/c are reconstructed for 7 TeV (8 TeV) data. At the hardware trigger stage, candidates are required to have a muon with high p_{T} or a hadron, photon or electron with high transverse energy. The software trigger requires a two-, three-, or four-track secondary vertex with significant displacement from any PV consistent with the decay of a b hadron, or a two-track vertex with a significant displacement from any PV consistent with a $\bar{D}^0 \to K^+\pi^-$ decay. In both cases, at least one charged particle must have a transverse momentum $p_{\mathrm{T}} > 1.7$ GeV/c and must be inconsistent with originating from any PV. A multivariate algorithm [43] is used for the identification of secondary vertices consistent with the decay of a b hadron. Secondary vertices consistent with the decay of a $\bar{D}^0$ meson must satisfy additional selection criteria, based on the momenta and transverse momenta of the $\bar{D}^0$ decay products ($p > 5$ GeV/c and $p_{\mathrm{T}} > 800$ MeV/c), and on the consistency, as a loose requirement, of the $\bar{D}^0$ momentum vector with the direction formed by joining the PV and the B^0 vertex.

III. SELECTION CRITERIA AND MULTIVARIATE ANALYSIS

The signal selection proceeds in two main steps. First, the dominant background, consisting of candidates where the 3π system originates from the B^0 vertex, called *prompt* hereafter, is suppressed by applying a 3π detached-vertex requirement. Second, the double-charm background is suppressed using a multivariate analysis (MVA). This is the only background with the same vertex topology as the signal.

This section is organized as follows. After a summary of the principles of the signal selection in Sec. III A, the categorization of the remaining background processes is given in Secs. III A 1 and III A 2. This categorization motivates (Sec. III A 3) the additional selection criteria that have to be applied to the tracks and vertices of the candidates in order to exploit the requirement of vertex detachment in its full power. Section III B describes the isolation tools used to take advantage of the fact that, for the $\tau^+ \to 3\pi\bar{\nu}_\tau$ channel, there is no other charged or neutral particle at the B^0 vertex beside the reconstructed particles in the final state. Particle identification requirements are presented in Sec. III C. The selection used for the normalization channel is described in Sec. III D. Section III E details the kinematic techniques used to reconstruct the decay chains in the signal and background hypotheses. Finally, the MVA that is used to reduce the double-charm backgrounds is presented in Sec. III F and, in Sec. III G, the background composition at various stages of the selection process is illustrated.

A. The detached-vertex topology

The signal final state consists of a D^{*-} meson, reconstructed in the $D^{*-} \to \bar{D}^0\pi^-$, $\bar{D}^0 \to K^+\pi^-$ decay chain, associated with a 3π system. The selection of D^{*-} candidates starts by requiring $\bar{D}^0$ candidates with masses between 1845 and 1885 MeV/c^2, p_{T} larger than 1.6 GeV/c, combined with pions of p_{T} larger than 0.11 GeV/c such that the difference between the D^{*-} and the $\bar{D}^0$ masses lies between 143 and 148 MeV/c^2. The $D^{*-}3\pi$ combination is very common in B meson decays, with a signal-to-background ratio smaller than 1%. The dominant background is prompt, i.e. consisting of candidates where the 3π system is produced at the B^0 vertex. However, in the signal case, because of the significant τ lifetime and boost along the forward direction, the 3π system is detached from the B^0 vertex, as shown in Fig. 1. The requirement for the detached vertex is that the distance between the 3π and the B^0 vertices along the beam direction, $\Delta z \equiv z(3\pi) - z(B^0)$, is greater than four times its uncertainty, $\sigma_{\Delta z}$. This leads to an improvement in the signal to noise ratio by a factor 160, as shown in Fig. 2. The remaining background consists of two main categories: candidates with a true detached-vertex topology and candidates that appear to have such a detached-vertex topology.

1. Background with detached-vertex topology

The double-charm $B \to D^{*-}D(X)$ decays are the only other B decays with the same vertex topology as the signal. Figure 2 shows, on simulated events, the dominance of the

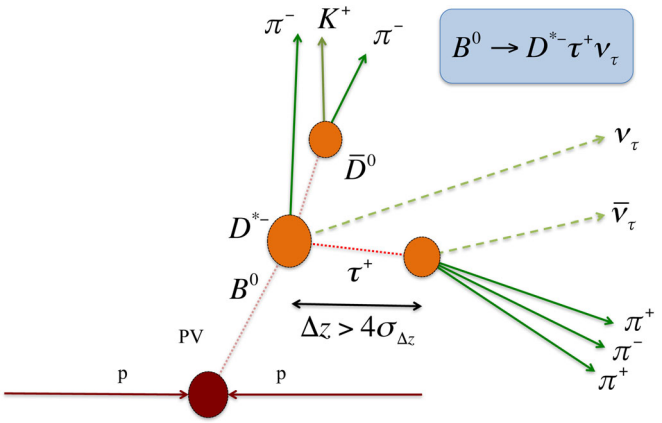

FIG. 1. Topology of the signal decay. A requirement on the distance between the 3π and the B^0 vertices along the beam direction to be greater than four times its uncertainty is applied.

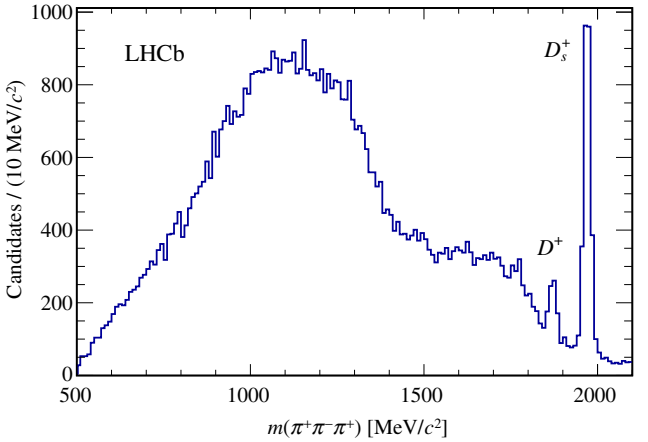

FIG. 3. Distribution of the 3π mass for candidates after the detached-vertex requirement. The D^+ and D_s^+ mass peaks are indicated.

double-charm background over the signal after the detached-vertex requirement. Figure 3 shows the 3π mass data distribution after the detached-vertex requirement, where peaking structures corresponding to the $D^+ \to 3\pi$ decay and $D_s^+ \to 3\pi$ decay—a very important control channel for this analysis—are clearly visible.

2. Background from other sources

Requirements additional to the detached vertex are needed to reject spurious background sources with vertex topologies similar to the signal. The various background sources are classified to distinguish candidates where the 3π system originates from a common vertex and those where one of the three pions originates from a different vertex.

The background category, where the 3π system stems from a common vertex, is further divided into two different classes depending on whether or not the D^{*-} and 3π system

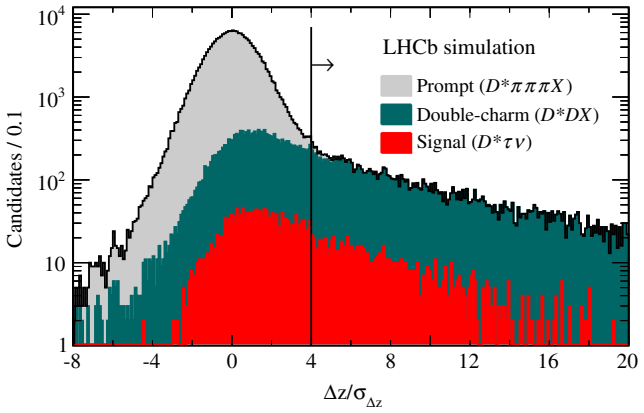

FIG. 2. Distribution of the distance between the B^0 vertex and the 3π vertex along the beam direction, divided by its uncertainty, obtained using simulation. The vertical line shows the 4σ requirement used in the analysis to reject the prompt background component.

originate from the same b hadron. In the first case, the 3π system either comes from the decay of a τ lepton or a D^0, D^+, D_s^+ or Λ_c^+ hadron. Candidates originating from b baryons form only 2% of this double-charm category. In this case, the candidate has the correct signal-like vertex topology. Alternatively, it comes from a misreconstructed prompt background candidate containing a B^0, B^+, B_s^0 or Λ_b^0 hadron. The detailed composition of these different categories at the initial and at the final stage of the analysis is described in Sec. III G. In the second case, the D^{*-} and the 3π systems are not daughters of the same b hadron. The 3π system originates from one of the following sources: the other b hadron present in the event (*B1B2* category); the decay of charm hadrons produced at the PV (*charm* category); another PV; or an interaction in the beam pipe or in the detector material.

The 3π background not originating from the same vertex is dominated by candidates where two pions originate from the same vertex whilst the third may come directly from the PV, from a different vertex in the decay chain of the same b hadron, from the other b hadron produced at the PV, or from another PV. Due to the combinatorial origin of this background, there is no strong correlation between the charge of the 3π system and the D^{*-} charge. This enables the normalization of the combinatorial background with the wrong-sign data sample.

3. Summary of the topological selection requirements

The requirements applied to suppress combinatorial and charm backgrounds, in addition to the detached-vertex criterion, are reported in Table I. These include a good track quality and a minimum transverse momentum of 250 MeV/c for each pion, a good vertex reconstruction quality for the 3π system and large $\chi^2_{\rm IP}$ with respect to any PV for each pion of the 3π system and for the $\bar{D}^0$ candidate, where $\chi^2_{\rm IP}$ is defined as the difference in the vertex-fit χ^2 of a

TABLE I. List of the selection cuts. See text for further explanation.

Variable	Requirement	Targeted background
$[z(3\pi) - z(B^0)]/\sigma_{(z(3\pi)-z(B^0))}$	> 4	Prompt
p_T (π), π from 3π	> 250 MeV/c	All
3π vertex χ^2	< 10	Combinatorial
$\chi^2_{IP}(\pi)$, π from 3π	> 15	Combinatorial
$\chi^2_{IP}(\bar{D}^0)$	> 10	Charm
$[z(3\pi) - z(\mathrm{PV})]/\sigma_{(z(3\pi)-z(\mathrm{PV}))}$	> 10	Charm
$r_{3\pi}$	$\in [0.2, 5.0]$ mm	Spurious 3π
$\mathrm{PV}(\bar{D}^0)$	$= \mathrm{PV}(3\pi)$	Charm/combinatorial
Number of B^0 candidates	$= 1$	All
$\Delta m \equiv m(D^{*-}) - m(\bar{D}^0)$	$\in [143, 148]$ MeV/c^2	Combinatorial

given PV reconstructed with and without the particle under consideration. In addition, the 3π vertex must be detached from its primary vertex along the beam axis by at least 10 times the corresponding uncertainty. The distance from the 3π vertex position to the beam center in the plane transverse to the beam direction, $r_{3\pi}$, must be outside the beam envelope and inside the beam pipe to avoid 3π vertices coming from proton interactions or secondary interactions with the beam-pipe material. The attached primary vertex to the $\bar{D}^0$ and 3π candidates must be the same. The number of candidates per event must be equal to one; this cut is the first rejection step against nonisolated candidates. Finally, the difference between the reconstructed D^{*-} and $\bar{D}^0$ masses must lie between 143 and 148 MeV/c^2.

B. Isolation requirements

1. Charged isolation

A charged-isolation algorithm ensures that no extra tracks are compatible with either the B^0 or 3π decay vertices. It is implemented by counting the number of charged tracks having p_T larger than 250 MeV/c, χ^2_{IP} with respect to the PV larger than 4, and $\chi^2_{IP}(3\pi)$ and $\chi^2_{IP}(B^0)$, with respect to the vertex of the 3π and B^0 candidates, respectively, smaller than 25. The $D^{*-}3\pi$ candidate is rejected if any such track is found. As an example, the performance of the charged-isolation algorithm is determined on a simulated sample of double-charm decays with a D^0 meson in the final state. In cases where $B^0 \to D^{*-}D^0K^+(X)$, with $D^0 \to K^-3\pi(X)$, two charged kaons are present in the decay chain, one originating from the B^0 vertex and the other from the D^0 vertex. For these candidates, the rejection rate is 95%. The charged-isolation algorithm has a selection efficiency of 80% on a data sample of exclusive $B^0 \to D^{*-}3\pi$ decays. This sample has no additional charged tracks from the B^0 vertex and has thus similar charged-isolation properties as the signal. This value is in good agreement with the efficiency determined from simulation.

Reversing the isolation requirement provides a sample of candidates from the inclusive D^0 decay chain mentioned above, where a D^0 meson decays into $K^-3\pi$ and the charged kaon has been found as a nearby track. Figure 4 shows the $K^-3\pi$ mass distribution featuring a prominent D^0 peak. This control sample is used to determine the properties of the $B \to D^{*-}D^0(X)$ background in the signal fit.

2. Neutral isolation

Background candidates from decays with additional neutral particles are suppressed by using the energy deposited in the electromagnetic calorimeter in a cone of 0.3 units in $\Delta\eta - \Delta\phi$ around the direction of the 3π system, where ϕ is the azimuthal angle in the plane perpendicular to the beam axis. For this rejection method to be effective, the amount of collected energy in the region of interest must be small when no neutral particles are produced in the B^0 meson decay. Candidates where the B^0 meson decays to $D^{*-}3\pi$, with $D^{*-} \to \bar{D}^0\pi^-$, are used as a check. Figure 5 compares the distributions of the $D^{*-}3\pi$ mass with and without the requirement of an energy deposition of at least 8 GeV in the electromagnetic calorimeter around the 3π direction. Since it is known that no neutral particle is emitted in this decay, the inefficiency of this rejection method is estimated by the ratio of the yields of the two

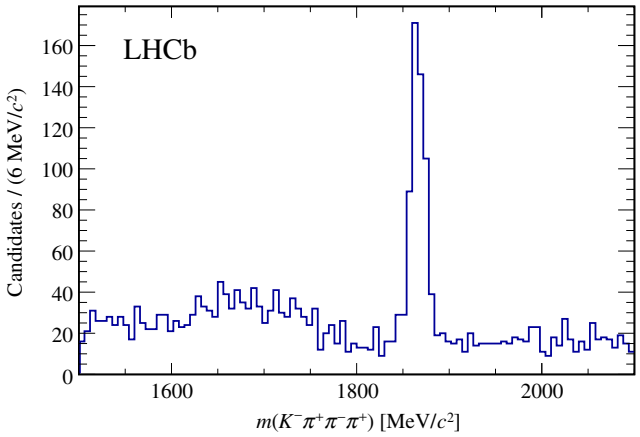

FIG. 4. Distribution of the $K^-3\pi$ mass for D^0 candidates where a charged kaon has been associated to the 3π vertex.

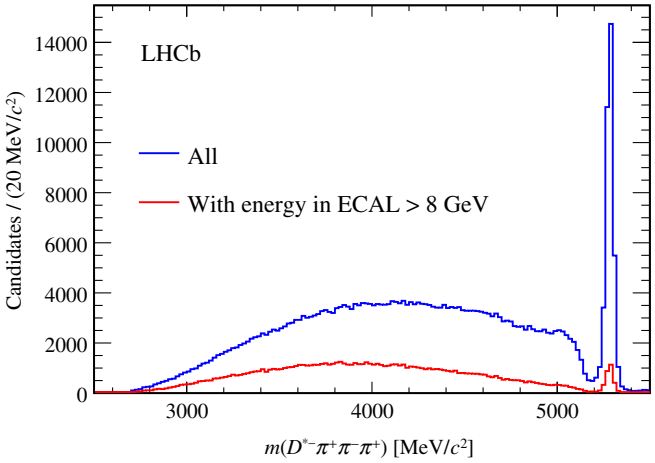

FIG. 5. Distribution of the $D^{*-}3\pi$ mass (blue) before and (red) after a requirement of finding an energy of at least 8 GeV in the electromagnetic calorimeter around the 3π direction.

spectra within ± 30 MeV$/c^2$ around the B^0 mass, and it is found to be small enough to allow the use of this method. The energy deposited in the electromagnetic calorimeter around the 3π direction is one of the input quantities to the MVA described below, used to suppress inclusive D_s^+ decays to $3\pi X$, which contain photons and π^0 mesons in addition to the three pions. Photons are also produced when D_s^+ excited states decay to the D_s^+ ground state. The use of this variable has an impact on signal, since it vetoes the $\tau^+ \to 3\pi\pi^0\bar{\nu}_\tau$ decay, whose efficiency is roughly one half with respect to that of the 3π mode, as can be seen later in Table II.

C. Particle identification requirements

In order to ensure that the tracks forming the 3π candidate are real pions, a positive pion identification is required and optimized taking into account the efficiency and rejection performance of particle identification (PID) algorithms, and the observed kaon to pion ratio in the 3π candidates, as measured through the D^- peak when giving a kaon mass to the negatively charged pion. As a result, the kaon identification probability is required to be less than 17%. To keep the D^{*-} reconstruction efficiency as high as possible, the requirement on the kaon identification probability for the soft-momentum pion originating from the D^{*-} decay is set to be less than 50%. The $D^+ \to K^-\pi^+\pi^+$ and $D^+ \to K^-\pi^+\pi^+\pi^0$ decays have large branching fractions and contribute to the $B \to D^{*-}D^+(X)$ background, that is significant when the kaon is misidentified as a pion. A remaining kaon contamination of about 5% in the final sample is estimated by studying the $K^-\,\pi^+\,\pi^+$ mass when assigning the kaon mass to the negative pion. Figure 6 shows the $K^-\,\pi^+\,\pi^+$ mass distribution for candidates that have passed all analysis requirements, except that the π^- candidate must have a high kaon identification probability. A clear D^+ signal of 740 ± 30 candidates is visible, with little combinatorial background. Therefore, an additional requirement on the kaon identification probability of the π^- candidate is applied. All of these PID requirements are chosen in order to get the best discrimination between signal and background. They form, together with the topology selection and the isolation requirement defined above, the final selection.

D. Selection of the normalization channel

The $B^0 \to D^{*-}3\pi$ normalization channel is selected by requiring the $\bar{D}^0$ vertex to be located at least 4σ downstream of the 3π vertex along the beam direction, where σ is the distance between the B^0 and $\bar{D}^0$ vertices divided by their uncertainties added in quadrature. All other selection criteria are identical to that of the signal case, except for the fact that no MVA requirement is applied to the normalization channel. Figure 7 shows the $D^{*-}3\pi$ mass spectrum after all these requirements. Moreover, the high purity of this sample of exclusive B^0 decays allows the

TABLE II. Summary of the efficiencies (in %) measured at the various steps of the analysis for simulated samples of the $B^0 \to D^{*-}3\pi$ channel and the $B^0 \to D^{*-}\,\tau^+\,\nu_\tau$ signal channel for both τ decays to $3\pi\,\bar{\nu}_\tau$ and $3\pi\,\pi^0\,\bar{\nu}_\tau$ modes. No requirement on the BDT output is applied for $D^{*-}3\pi$ candidates. The relative efficiency designates the individual efficiency of each requirement.

	Absolute efficiencies (%)			Relative efficiencies (%)		
		$D^{*-}\,\tau^+\,\nu_\tau$			$D^{*-}\,\tau^+\,\nu_\tau$	
Requirement	$D^{*-}3\pi$	$3\pi\,\bar{\nu}_\tau$	$3\pi\,\pi^0\,\bar{\nu}_\tau$	$D^{*-}3\pi$	$3\pi\,\bar{\nu}_\tau$	$3\pi\,\pi^0\,\bar{\nu}_\tau$
Geometrical acceptance	14.65	15.47	14.64			
After:						
Initial selection	1.382	0.826	0.729			
Spurious 3π removal	0.561	0.308	0.238	40.6	37.3	32.6
Trigger requirements	0.484	0.200	0.143	86.3	65.1	59.9
Vertex selection	0.270	0.0796	0.0539	55.8	39.8	37.8
Charged isolation	0.219	0.0613	0.0412	81.2	77.0	76.3
BDT requirement		0.0541	0.0292		94.1	74.8
PID requirements	0.136	0.0392	0.0216	65.8	72.4	74.1

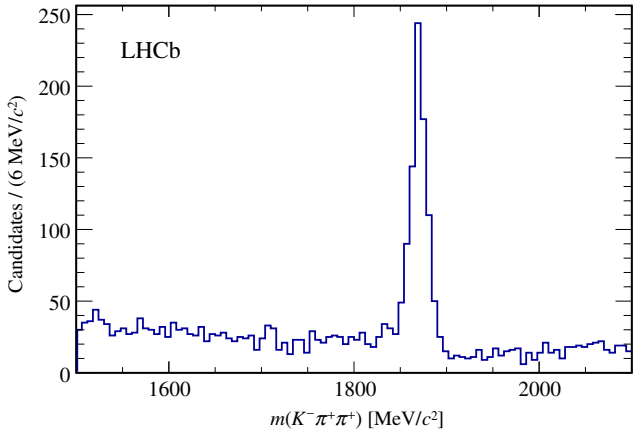

FIG. 6. Distribution of the $K^-\ \pi^+\ \pi^+$ mass for D^+ candidates passing the signal selection, where the negative pion has been identified as a kaon and assigned the kaon mass.

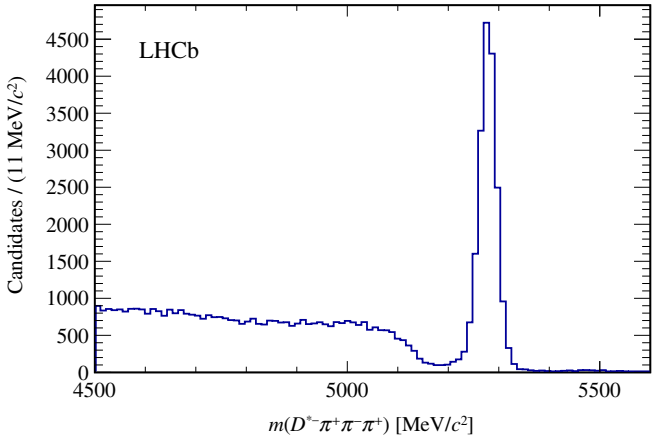

FIG. 7. Distribution of the $D^{*-}3\pi$ mass for candidates passing the selection.

validation of the selection efficiencies derived using simulation.

E. Reconstruction of the decay kinematics

Due to the precise knowledge of the $\bar{D}^0$, 3π and B^0 decay vertices, it is possible to reconstruct the decay chains of both signal and background processes, even in the presence of unreconstructed particles, such as two neutrinos in the case of the signal, or neutral particles originating at the 3π vertex in the case of double-charm background. The relevant reconstruction techniques are detailed in the following.

1. Reconstruction in the signal hypothesis

The missing information due to the two neutrinos emitted in the signal decay chain can be recovered with the measurements of the B^0 and τ line of flight (unit vectors joining the B^0 vertex to the PV and the 3π vertex to the B^0 vertex, respectively) together with the known B^0 and τ masses. The reconstruction of the complete decay kinematics of both the B^0 and τ decays is thus possible, up to two two-fold ambiguities.

The τ momentum in the laboratory frame is obtained as (in units where $c = 1$)

$$|\vec{p}_\tau| = \frac{(m_{3\pi}^2 + m_\tau^2)|\vec{p}_{3\pi}|\cos\theta_{\tau,3\pi} \pm E_{3\pi}\sqrt{(m_\tau^2 - m_{3\pi}^2)^2 - 4m_\tau^2|\vec{p}_{3\pi}|^2\sin^2\theta_{\tau,3\pi}}}{2(E_{3\pi}^2 - |\vec{p}_{3\pi}|^2\cos^2\theta_{\tau,3\pi})}, \tag{4}$$

where $\theta_{\tau,3\pi}$ is the angle between the 3π system three-momentum and the τ line of flight; $m_{3\pi}$, $|\vec{p}_{3\pi}|$ and $E_{3\pi}$ are the mass, three-momentum and energy of the 3π system, respectively; and m_τ is the known τ mass. Equation (4) yields a single solution, in the limit where the opening angle between the 3π and the τ directions takes the maximum allowed value

$$\theta_{\tau,3\pi}^{\max} = \arcsin\left(\frac{m_\tau^2 - m_{3\pi}^2}{2m_\tau|\vec{p}_{3\pi}|}\right). \tag{5}$$

At this value, the argument of the square root in Eq. (4) vanishes, leading to only one solution, which is used as an estimate of the τ momentum. The same procedure is applied to estimate the B^0 momentum

$$|\vec{p}_{B^0}| = \frac{(m_Y^2 + m_{B^0}^2)|\vec{p}_Y|\cos\theta_{B^0,Y} \pm E_Y\sqrt{(m_{B^0}^2 - m_Y^2)^2 - 4m_{B^0}^2|\vec{p}_Y|^2\sin^2\theta_{B^0,Y}}}{2(E_Y^2 - |\vec{p}_Y|^2\cos^2\theta_{B^0,Y})}, \tag{6}$$

by defining

$$\theta_{B^0,Y}^{\max} = \arcsin\left(\frac{m_{B^0}^2 - m_Y^2}{2m_{B^0}|\vec{p}_Y|}\right), \tag{7}$$

where Y represents the $D^{*-}\tau$ system. Here, the three-momentum and mass of the $D^{*-}\tau$ system are calculated using the previously estimated τ momentum

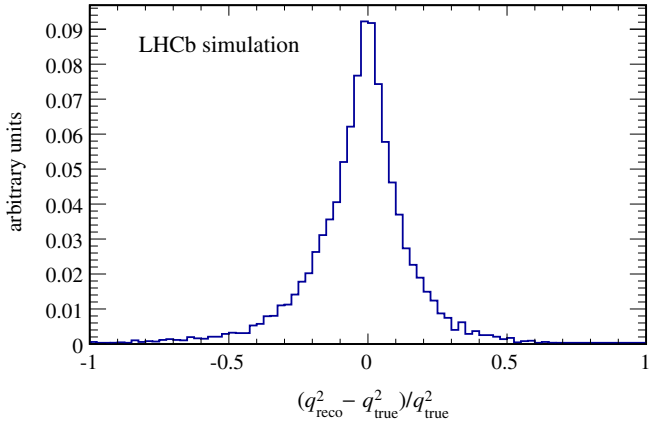

FIG. 8. Difference between the reconstructed and true q^2 variables divided by the true q^2, observed in the $B^0 \to D^{*-}\tau^+\nu_\tau$ simulated signal sample after partial reconstruction.

$$\vec{p}_Y = \vec{p}_{D^{*-}} + \vec{p}_\tau, \qquad E_Y = E_{D^{*-}} + E_\tau, \tag{8}$$

where $\vec{p}_{D^{*-}}$ and $\vec{p}_\tau$ are the three-momenta of the D^{*-} and the τ candidates, and $E_{D^{*-}}$ and E_τ their energies. Using this method, the rest frame variables $q^2 \equiv (p_{B^0} - p_{D^{*-}})^2 = (p_\tau + p_{\nu_\tau})^2$ and the τ decay time, t_τ, are determined with sufficient accuracy to retain their discriminating power against double-charm backgrounds, as discussed in Sec. V. Figure 8 shows the difference between the reconstructed and the true value of q^2 divided by the true q^2 on simulated events. No significant bias is observed and an average resolution of 1.2 GeV$^2/c^4$ is obtained. The relative q^2 resolution is 18% full-width half-maximum. The slight asymmetry is due to the presence at low q^2 of a tail of reconstructed q^2 below the kinematical limit for true q^2.

2. Reconstruction assuming a double-charm origin for the candidate

A full kinematic reconstruction of the B decay chain specifically adapted to two-body double-charm B decays provides additional discrimination. After the detached-vertex requirement, the main source of background candidates is attributed to decays of the form $B \to D^{*-}D_s^+(X)$, with $D_s^+ \to 3\pi N$, N being a system of unreconstructed neutral particles. For these decays, the missing information is due to a neutral system of unknown mass originating from the D_s^+ decay vertex, i.e. four unknowns. The measurements of the B^0 and D_s^+ lines of flight, providing four constraints, together with the known B^0 mass, are sufficient to reconstruct the full decay kinematics

$$|\vec{p}_B|\hat{u}_B = |\vec{p}_{D_s^+}|\hat{u}_{D_s^+} + \vec{p}_{D^{*-}}. \tag{9}$$

This equation assumes the absence of any other particles in the B decay. It is however also valid when an additional particle is aligned with the D_s^+ momentum direction, as in the case of $B^0 \to D^{*-}\, D_s^{*+}$, where the soft photon emitted in the D_s^{*+} decay has a very low momentum in the direction transverse to that of the D_s^+ momentum. It is also a good approximation for quasi-two-body B^0 decays to D^{*-} and higher excitations of the D_s^+ meson. This equation can be solved with two mathematically equivalent ways, through a vectorial or scalar product methods, noted v and s respectively. This equivalence does not hold in the presence of extra particles. This difference is used to provide some further discrimination between signal and nonisolated backgrounds. The magnitudes of the momenta obtained for each method are:

$$P_{B,v} = \frac{|\vec{p}_{D^{*-}} \times \hat{u}_{D_s^+}|}{|\hat{u}_B \times \hat{u}_{D_s^+}|}, \tag{10a}$$

$$P_{B,s} = \frac{\vec{p}_{D^{*-}} \cdot \hat{u}_B - (\vec{p}_{D^{*-}} \cdot \hat{u}_{D_s^+})(\hat{u}_B \cdot \hat{u}_{D_s^+})}{1 - (\hat{u}_B \cdot \hat{u}_{D_s^+})^2}, \tag{10b}$$

for the B^0 momentum, and

$$P_{D_s,v} = \frac{|\vec{p}_{D^{*-}} \times \hat{u}_B|}{|\hat{u}_{D_s^+} \times \hat{u}_B|}, \tag{11a}$$

$$P_{D_s,s} = \frac{(\vec{p}_{D^{*-}} \cdot \hat{u}_B)(\hat{u}_B \cdot \hat{u}_{D_s^+}) - \vec{p}_{D^{*-}} \cdot \hat{u}_{D_s^+}}{1 - (\hat{u}_B \cdot \hat{u}_{D_s^+})^2}, \tag{11b}$$

for the D_s^+ momentum.

Since this partial reconstruction works without imposing a mass to the $3\pi N$ system, the reconstructed $3\pi N$ mass can be used as a discriminating variable. Figure 9 shows the $3\pi N$ mass distribution obtained on a sample enriched in $B \to D^{*-}D_s^+(X)$ decays, with $D_s^+ \to 3\pi N$, by means of the output of the MVA (see Sec. III F). A peaking structure originating from D_s^+ and D_s^{*+} decays is also present around 2000 MeV$/c^2$. Due to the presence of two neutrinos at different vertices, signal decays are not handled as well by this partial reconstruction method, which therefore provides a useful discrimination between signal and background due to $B \to D^{*-}D_s^+(X)$ decays. However, this method cannot discriminate the signal from double-charm backgrounds due to $B \to D^{*-}D^0(X)$ and $B \to D^{*-}D^+(X)$ decays, where two kaons are missing at the B^0 and 3π vertices.

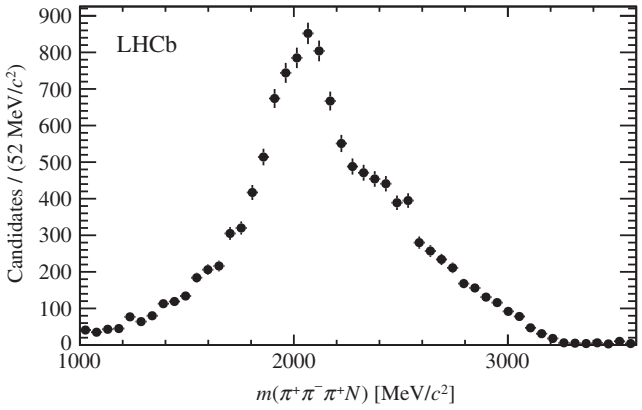

FIG. 9. Distribution of the reconstructed $3\pi N$ mass observed in a data sample enriched by $B \to D^{*-}D_s^+(X)$ candidates.

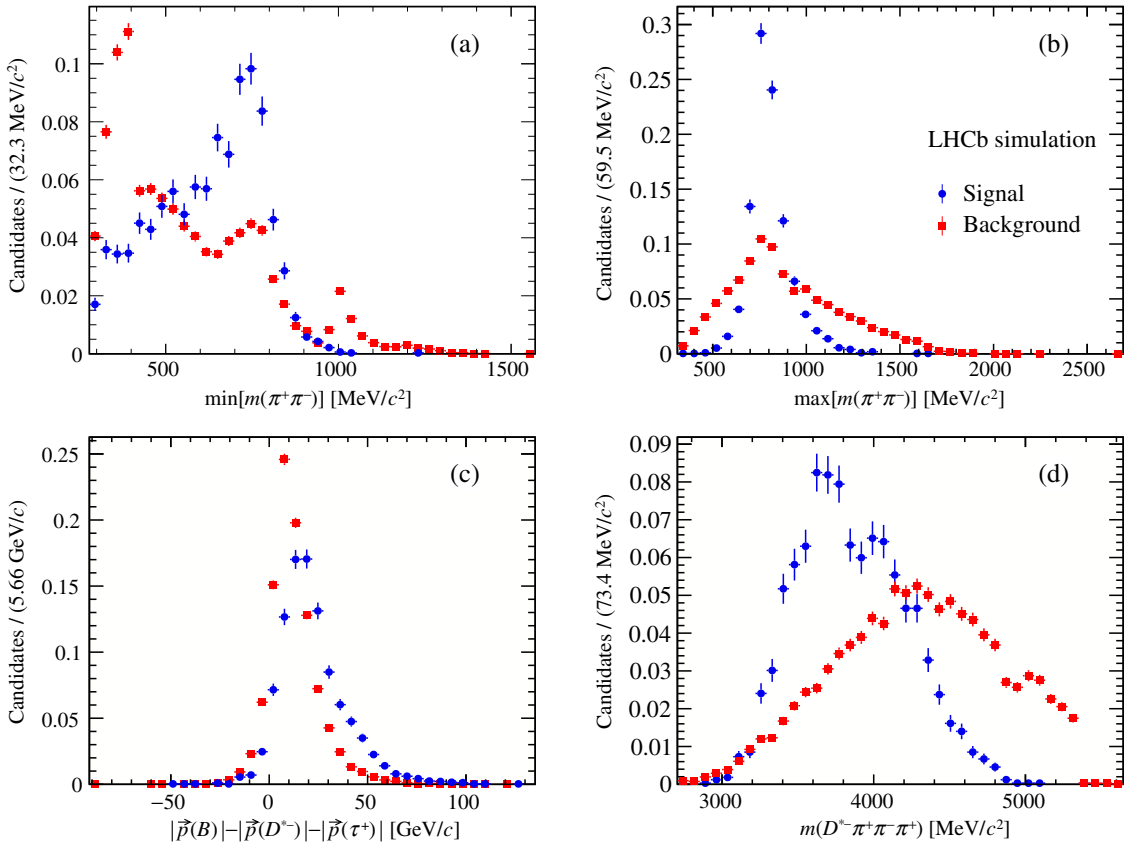

FIG. 10. Normalized distributions of (a) min$[m(\pi^+\pi^-)]$, (b) max$[m(\pi^+\pi^-)]$, (c) approximated neutrino momentum reconstructed in the signal hypothesis, and (d) the $D^{*-}3\pi$ mass in simulated samples.

F. Multivariate analysis

Three features are used to reject the double-charm background: the different resonant structures of $\tau^+ \to 3\pi\bar{\nu}_\tau$ and $D_s^+ \to 3\pi X$ decays, the neutral isolation and the different kinematic properties of signal and background candidates. The latter feature is exploited by using the reconstruction techniques described in Sec. III E.

To suppress double-charm background, a set of 18 variables is used as input to a MVA based upon a boosted decision tree (BDT) [44,45]. This set is as follows: the output variables of the neutral isolation algorithm; momenta, masses and quality of the reconstruction of the decay chain under the signal and background hypotheses; the masses of oppositely charged pion pairs, the energy and the flight distance in the transverse plane of the 3π system; the mass of the six-charged-tracks system. The BDT is trained using simulated samples of signal and double-charm background decays. Figure 10 shows the normalized distributions of the four input variables having the largest discriminating power for signal and background: the minimum and maximum of the masses of oppositely charged pions, min$[m(\pi^+\pi^-)]$ and max$[m(\pi^+\pi^-)]$; the neutrino momentum, approximated as the difference of the modulus of the momentum of the B^0 and the sum of the moduli of the momenta of D^{*-} and τ reconstructed in the signal hypothesis; and the $D^{*-}3\pi$ mass. The BDT response for signal and background is illustrated in Fig. 11.

The $B \to D^{*-}D_s^+(X)$, $B \to D^{*-}D^0(X)$ and $B \to D^{*-}D^+(X)$ control samples, described in Sec. IV, are used to validate the BDT. Good agreement between simulation and control samples is observed both for the BDT response and the distributions of the input variables.

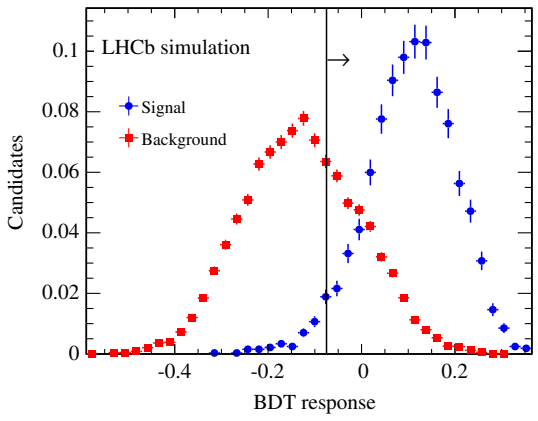

FIG. 11. Distribution of the BDT response on the signal and background simulated samples.

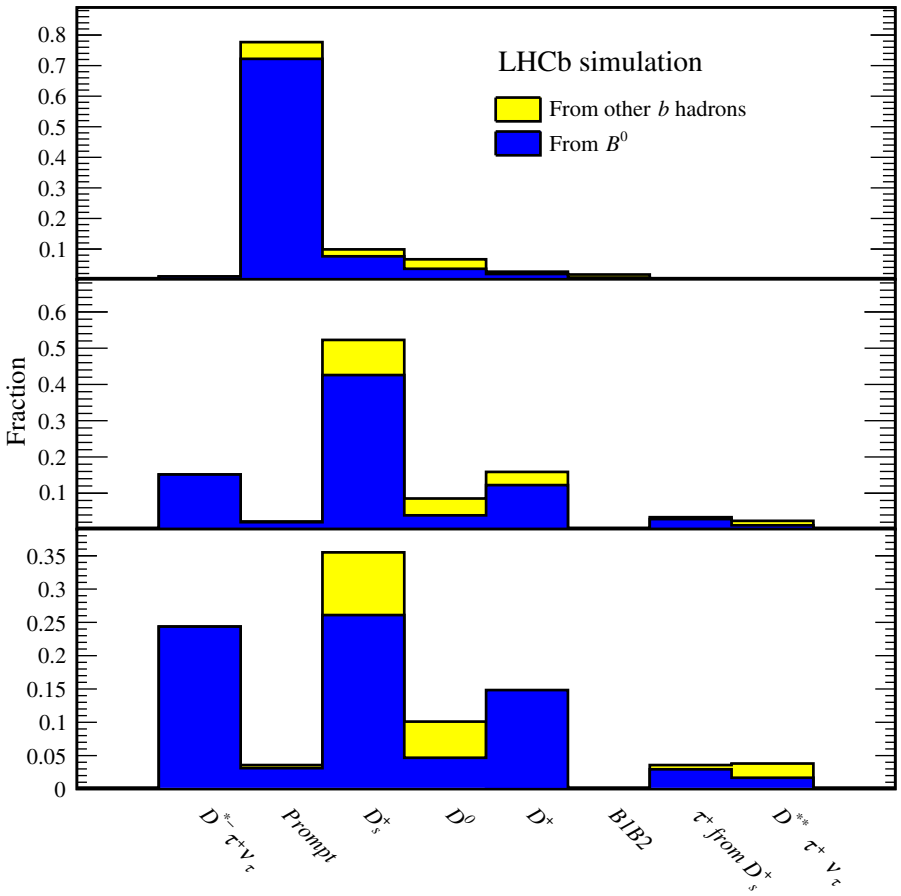

FIG. 12. Composition of an inclusive simulated sample where a D^{*-} and a 3π system have been produced in the decay chain of a $b\,\bar{b}$ pair from a pp collision. Each bin shows the fractional contribution of the different possible parents of the 3π system (blue from a B^0, yellow for other b hadrons): from signal; directly from the b hadron (prompt); from a charm parent D_s^+, D^0, or D^+ meson; 3π from a B and the D^0 from the other B ($B1B2$); from τ lepton following a D_s^+ decay; from a τ lepton following a $D^{**}\tau^+\nu_\tau$ decay (D^{**} denotes here any higher excitation of D mesons). (Top) After the initial selection and the removal of spurious 3π candidates. (Middle) For candidates entering the signal fit. (Bottom) For candidates populating the last 3 bins of the BDT distribution (cf. Fig. 16).

The signal yield is determined from candidates in the region where the BDT output is greater than -0.075. According to simulation, this value gives the best statistical power in the determination of the signal yield. Candidates with the BDT output less than -0.075 are highly enriched in D_s^+ decays and contain very little signal, as shown in Fig. 11, and represent about half of the total data sample. They are used to validate the simulation of the various components in $D_s^+ \to 3\pi X$ decays used in the parametrization of the templates entering in the fit that determines the signal yield, as explained in Sec. IV A. No BDT cut is applied in the selection for the normalization channel.

G. Composition of the selected sample and selection efficiencies

Figure 12 shows the composition of an inclusive sample of simulated events, generated by requiring that a D^{*-} meson and a 3π system are both part of the decay chain of a $b\,\bar{b}$ pair produced in a proton-proton collision before the detached-vertex requirement, at the level of the signal fit, and with a tighter cut corresponding to the last three BDT bins of Fig. 16. In the histograms, the first bin corresponds to the signal, representing only 1% of the candidates at the initial stage, and the second bin to prompt candidates, where the 3π system originates from the b -hadron decay. It constitutes by far the largest initial background source. The following three bins correspond to cases where the 3π system originates from the decay of a D_s^+, D^0 or D^+ meson, respectively. The plot in the middle corresponds to the BDT output greater than -0.075 used in the analysis to define the sample in which the signal determination takes place. One can see the suppression of the prompt background due to the detached-vertex requirement, and the dominance of the D_s^+ background. The bottom plot shows for illustration the sample composition with the harder BDT output cut. The D_s^+ contribution is now suppressed as well. The signal fraction represents about 25% at this stage. Figure 12 also allows contributions due to decays of other b hadrons to be compared with those of B^0 mesons. Table II presents the efficiency of the various selection steps, both for signal and normalization channels.

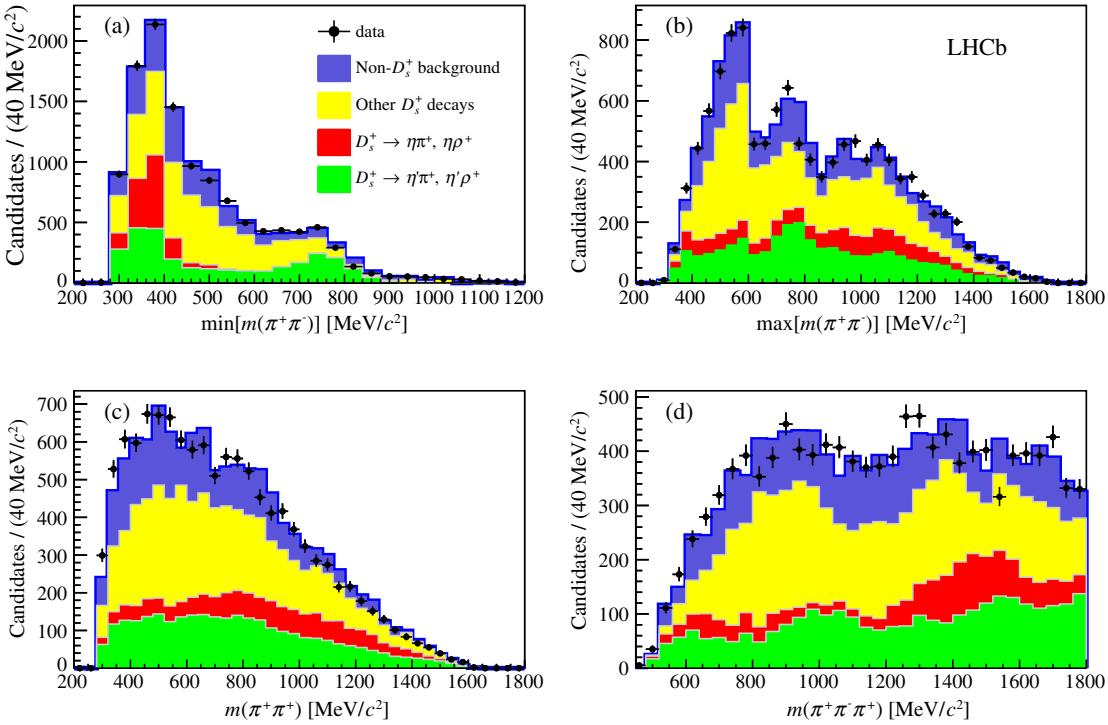

FIG. 13. Distributions of (a) min$[m(\pi^+\pi^-)]$, (b) max$[m(\pi^+\pi^-)]$, (c) $m(\pi^+\pi^+)$, (d) $m(\pi^+\pi^-\pi^+)$ for a sample enriched in $B \to D^{*-}D_s^+(X)$ decays, obtained by requiring the BDT output below a certain threshold. The different fit components correspond to D_s^+ decays with (red) η or (green) η' in the final state, (yellow) all the other considered D_s^+ decays, and (blue) backgrounds originating from decays not involving the D_s^+ meson.

The signal efficiency is computed from the efficiencies and abundances of the 3π and $3\pi\,\pi^0$ channels.

IV. STUDY OF DOUBLE-CHARM CANDIDATES

The fit that determines the signal yield uses templates that are taken from simulation. It is therefore of paramount importance to verify the agreement between data and simulation for the remaining background processes. Control samples from data are used wherever possible for this purpose. The relative contributions of double-charm backgrounds and their q^2 distributions from simulation are validated, and corrected where appropriate, by using data control samples enriched in such processes. Inclusive decays of D^0, D^+ and D_s^+ mesons to 3π are also studied in this way.

A. The D_s^+ decay model

The branching fraction of D_s^+ meson decays with a 3π system in the final state, denoted as $D_s^+ \to 3\pi X$ is about 15 times larger than that of the exclusive $D_s^+ \to 3\pi$ decay. This is due to the large contributions from decays involving intermediate states such as K_S^0, η, η', ϕ, and ω, which are generically denoted with the symbol R in the following. The branching fractions of processes of the type $D_s^+ \to R\pi^+$ are well known, but large uncertainties exist for several decays, such as $D_s^+ \to R(\to \pi^+\pi^- X)\pi^+\pi^0$ and $D_s^+ \to R3\pi$.

The τ lepton decays through the $a_1(1260)^+$ resonance, which leads to the $\rho^0\pi^+$ final state [36]. The dominant source of ρ^0 resonances in D_s^+ decays is due to $\eta' \to \rho^0\gamma$ decays. It is therefore crucial to control the η' contribution in D_s^+ decays very accurately. The η' contribution in the min$[m(\pi^+\pi^-)]$ distribution, obtained from simulation, is shown in Fig. 13. It exhibits a double peaking structure: at low mass, due to the endpoint of phase space for the charged pion pair in the $\eta \to \pi^+\pi^-\pi^0$ and $\eta' \to \eta\pi^+\pi^-$ decays and, at higher mass, a ρ^0 peak. The shape of this contribution is precisely known since the η' branching fractions are known to better than 2%. The precise measurement on data of the low-mass excess, which consists only of η' and η candidates, therefore enables the control of the η' contribution in the sensitive ρ region. The $D_s^+ \to 3\pi X$ decay model is determined from a data sample enriched in $B \to D^{*-}D_s^+(X)$ decays by requiring a low value of the BDT output. The distributions of min$[m(\pi^+\pi^-)]$ and max$[m(\pi^+\pi^-)]$, of the mass of the same-charge pions, $m(\pi^+\pi^+)$, and of the mass of the 3π system, $m(3\pi)$, are simultaneously fit with a model obtained from simulation. The fit model is constructed from the following components:

(i) D_s^+ decays where at least one pion originates from the decay of an η meson; the $D_s^+ \to \eta\pi^+$ and $D_s^+ \to \eta\rho^+$ components are in this category.
(ii) D_s^+ decays where, in analogy with the previous category, an η' meson is involved.
(iii) D_s^+ decays where at least one pion originates from an intermediate resonance other than η or η'; these

are then subdivided into $R\pi^+$ and $R\rho^+$ final states; these decays are dominated by $R = \omega, \phi$ resonances.

(iv) Other D_s^+ decays, where none of the three pions originates from an intermediate state; these are then subdivided into $K^0 3\pi$, $\eta 3\pi$, $\eta' 3\pi$, $\omega 3\pi$, $\phi 3\pi$, $\tau^+(\to 3\pi(N)\bar{\nu}_\tau)\nu_\tau$, and 3π nonresonant final states, $X_{\rm nr}$. Regarding the tauonic $D_s^+ \to \tau^+\nu_\tau$ decay, the label N stands for any potential extra neutral particle.

Templates for each category and for the non-D_s^+ candidates are determined from $B \to D^{*-}D_s^+(X)$ and $B \to D^{*-}3\pi X$ simulation samples, respectively. Figure 13 shows the fit results for the four variables. The fit measures the η and η' inclusive fractions very precisely because, in the $\min[m(\pi^+\pi^-)]$ histogram, the low-mass peak is the sum of the η and η' contributions, while only the η' meson contributes to the ρ^0 region. The ratio between decays with a π^+ and a ρ^+ meson in the final state is not precisely determined because of the limited sensitivity of the fit variables to the presence of the extra π^0. The sensitivity only comes from the low-yield high-mass tail of the 3π mass distribution which exhibits different endpoints for these two types of decays. Finally, the kinematical endpoints of the 3π mass for each $R3\pi$ final state enable the fit to determine their individual contributions, which are presently either poorly measured or not measured at all. The $D_s^+ \to \phi 3\pi$ and $D_s^+ \to \tau^+(\to 3\pi(N)\bar{\nu}_\tau)\nu_\tau$ branching fractions, known with a 10% precision, are fixed to their measured values [46].

The fit is in good agreement with the data, especially in the critical $\min[m(\pi^+\pi^-)]$ distribution. The χ^2 per degree of freedom of each fit is 0.91, 1.25, 1.1 and 1.45 for each histogram, respectively, when taking into account the simulation sample size. The fit parameters and their ratios, with values from simulation, are reported in Table III. These are used to correct the corresponding contributions from simulation. In the final fit performed in the high BDT output region, the shape of each contribution is scaled according to the ratio of candidates in the two BDT regions, which is taken from simulation.

The fit determines that $(47.3 \pm 2.5)\%$ of the D_s^+ decays in this sample contain η and η' mesons with an additional charged pion, $(20.6 \pm 4.0)\%$ contain ϕ and ω mesons with an additional charged pion and $(32.1 \pm 4.0)\%$ are due to $R3\pi$ modes. This last contribution is dominated by the $\eta 3\pi$ and $\eta' 3\pi$ modes. The large weighting factors observed in this D_s^+ decay-model fit correspond to channels whose branching fractions are not precisely known.

B. The $B \to D^{*-}D_s^+(X)$ control sample

Candidates where the D_s^+ meson decays exclusively to the $\pi^+\pi^-\pi^+$ final state give a pure sample of $B \to D^{*-}D_s^+(X)$ decays. This sample includes three types of processes[3]:

TABLE III. Results of the fit to the D_s^+ decay model. The relative contribution of each decay and the correction to be applied to the simulation are reported in the second and third columns, respectively.

D_s^+ decay	Relative contribution	Correction to simulation
$\eta\pi^+(X)$	0.156 ± 0.010	
$\eta\rho^+$	0.109 ± 0.016	0.88 ± 0.13
$\eta\pi^+$	0.047 ± 0.014	0.75 ± 0.23
$\eta'\pi^+(X)$	0.317 ± 0.015	
$\eta'\rho^+$	0.179 ± 0.016	0.710 ± 0.063
$\eta'\pi^+$	0.138 ± 0.015	0.808 ± 0.088
$\phi\pi^+(X), \omega\pi^+(X)$	0.206 ± 0.02	
$\phi\rho^+, \omega\rho^+$	0.043 ± 0.022	0.28 ± 0.14
$\phi\pi^+, \omega\pi^+$	0.163 ± 0.021	1.588 ± 0.208
$\eta 3\pi$	0.104 ± 0.021	1.81 ± 0.36
$\eta' 3\pi$	0.0835 ± 0.0102	5.39 ± 0.66
$\omega 3\pi$	0.0415 ± 0.0122	5.19 ± 1.53
$K^0 3\pi$	0.0204 ± 0.0139	1.0 ± 0.7
$\phi 3\pi$	0.0141	0.97
$\tau^+(\to 3\pi(N)\bar{\nu}_\tau)\nu_\tau$	0.0135	0.97
$X_{\rm nr} 3\pi$	0.038 ± 0.005	6.69 ± 0.94

(i) $B^0 \to D^{*-}D_s^{(*,**)+}$ decays, where a neutral particle is emitted in the decay of the excited states of the D_s^+ meson. The corresponding q^2 distribution peaks at the squared mass, $(p_{B^0} - p_{D^{*-}})^2$, of the given states.

(ii) $B_s^0 \to D^{*-}D_s^+X$ decays, where at least one additional particle is missing. This category contains feed-down from excited states, both for D^{*-} or D_s^+ mesons. The q^2 distribution is shifted to higher values.

(iii) $B^{0,-} \to D^{*-}D_s^+X^{0,-}$ decays, where at least one additional particle originates from either the $B^{0,-}$ decay, or the deexcitation of charm-meson resonances of higher mass, that results in a D^{*-} meson in the final state. These additional missing particles shift the q^2 distribution to even higher values.

The $B \to D^{*-}D_s^+(X)$ control sample is used to evaluate the agreement between data and simulation, by performing a fit to the distribution of the mass of the $D^{*-}3\pi$ system, $m(D^{*-}3\pi)$. The fitting probability density function $\mathcal{P}$ is parametrized as

$$\mathcal{P} = f_{\rm c.b.}\mathcal{P}_{\rm c.b.} + \frac{(1 - f_{\rm c.b.})}{k}\sum_j f_j \mathcal{P}_j, \qquad (12)$$

where $i, j = \{D_s^{*+}; D_s^+; D_{s0}^{*+}; D_{s1}^+; D_s^+X; (D_s^+X)_s\}$ and $k = \sum_i f_i$. The fraction of combinatorial background, $f_{\rm c.b.}$, is fixed in the fit. Its shape is taken from a sample where the D^{*-} meson and the 3π system have the same charge. Each component i is described by the probability density function $\mathcal{P}_i$, whose shapes are taken from simulation.

[3]In this section, D^{**} and D_s^{**} are used to refer to any higher-mass excitations of D^{*-} or D_s^+ mesons decaying to D^{*-} and D_s^+ ground states.

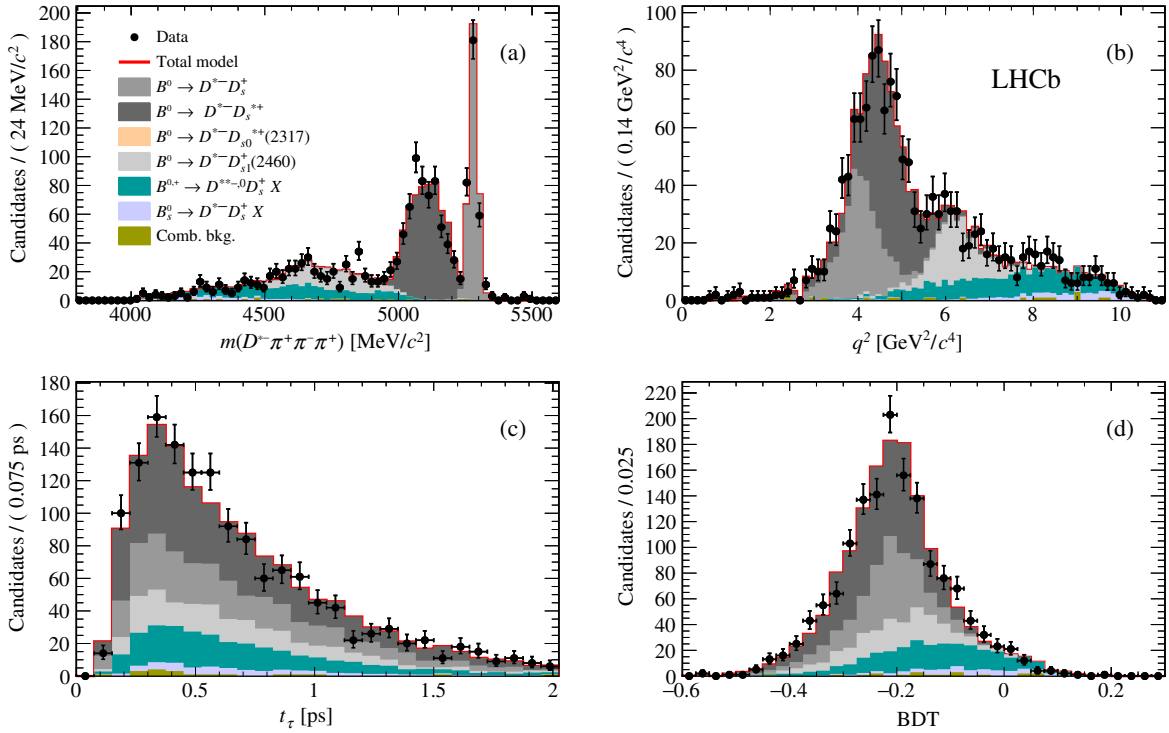

FIG. 14. Results from the fit to data for candidates containing a $D^{*-}D_s^+$ pair, where $D_s^+ \to 3\pi$. The fit components are described in the legend. The figures correspond to the fit projection on (a) $m(D^{*-}3\pi)$, (b) q^2, (c) 3π decay time t_τ and (d) BDT output distributions.

The parameters f_i are the relative yields of $B^0 \to D^{*-}D_s^+$, $B^0 \to D^{*-}D_{s0}^*(2317)^+$, $B^0 \to D^{*-}D_{s1}(2460)^+$, $B^{0,+} \to D^{*-}D_s^+X$ and $B_s^0 \to D^{*-}D_s^+X$ decays with respect to the number of $B^0 \to D^{*-}D_s^{*+}$ candidates. They are floating in the fit, and $f_{D_s^{*+}} = 1$ by definition.

The fit results are shown in Fig. 14 and reported in Table IV, where a comparison with the corresponding values in the simulation is also given, along with their ratios. The measured ratios, including the uncertainties and correlations, are used to constrain these contributions in the final fit. The large weighting factors observed in this fit correspond to channels whose branching fractions are not precisely known.

TABLE IV. Relative fractions of the various components obtained from the fit to the $B \to D^{*-}D_s^+(X)$ control sample. The values used in the simulation and the ratio of the two are also shown.

Parameter	Simulation	Fit	Ratio
$f_{\text{c.b.}}$	⋯	0.014	⋯
$f_{D_s^+}$	0.54	0.594 ± 0.041	1.10 ± 0.08
$f_{D_{s0}^{*+}}$	0.08	$0.000^{+0.040}_{-0.000}$	$0.00^{+0.50}_{-0.00}$
$f_{D_{s1}^+}$	0.39	0.365 ± 0.053	0.94 ± 0.14
$f_{D_s^+X}$	0.22	0.416 ± 0.069	1.89 ± 0.31
$f_{(D_s^+X)_s}$	0.23	0.093 ± 0.027	0.40 ± 0.12

C. The $B \to D^{*-}D^0(X)$ and $B \to D^{*-}D^+(X)$ control samples

The decays of D^0 and D^+ mesons into final states with three pions are dominated by the $D^{0,+} \to K^{-,0}3\pi(\pi^0)$ modes, whose subresonant structure is known. The agreement between data and simulation is validated in the D^0 case by using a control sample. The isolation algorithm identifies a kaon with charge opposite to the total charge of the 3π system, and compatible with originating from the 3π vertex.

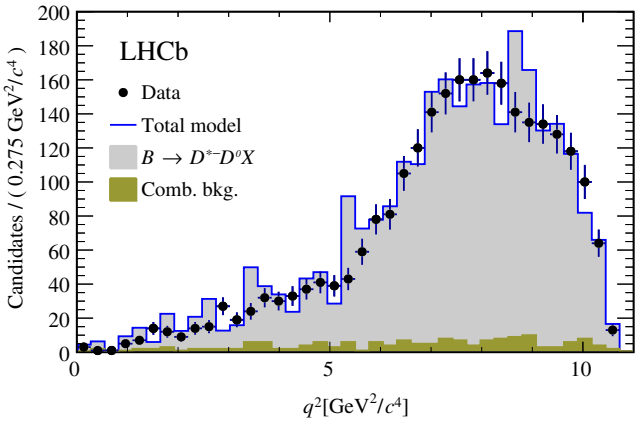

FIG. 15. Distribution of q^2 for candidates in the $B \to D^{*-}D^0(X)$ control sample, after correcting for the disagreement between data and simulation.

The mass of the $K^-3\pi$ system must be compatible with the known D^0 mass. Disagreement between data and simulation is found in the q^2 and D^{*-} D^0 mass distributions and corrected for. Figure 15 shows the q^2 distribution after this correction.

A pure sample of $B \to D^{*-}D^+(X)$ decays is obtained by inverting the PID requirements on the negative pion of the 3π system, assigning to this particle the kaon mass and selecting 3π candidates with mass compatible with the known D^+ mass. As in the $B \to D^{*-}D^0(X)$ control sample, disagreement between data and simulation is found. The limited size of this sample does not allow the determination of a specific correction. The same correction found in the $B \to D^{*-}D^0(X)$ case is therefore applied, since the dominant decay $B \to D^{*-}DK$ is identical for both cases.

V. DETERMINATION OF THE SIGNAL YIELD

The yield of $B^0 \to D^{*-}\tau^+\nu_\tau$ decays is determined from a three-dimensional binned maximum likelihood fit to the distributions of q^2, 3π decay time, and BDT output. Signal and background templates are produced with eight bins in q^2, eight bins in t_τ, and four bins in the BDT output, from the corresponding simulation samples. The model used to fit the data is summarized in Table V. In the table,

(i) $N_{\rm sig}$ is a free parameter accounting for the yield of signal candidates.

(ii) $f_{\tau\to 3\pi\nu}$ is the fraction of $\tau^+ \to 3\pi\bar{\nu}_\tau$ signal candidates with respect to the sum of the $\tau^+ \to 3\pi\bar{\nu}_\tau$ and $\tau^+ \to 3\pi\pi^0\bar{\nu}_\tau$ components. This parameter is fixed to 0.78, according to the different branching fractions and efficiencies of the two modes.

(iii) $f_{D^{**}\tau\nu}$, fixed to 0.11, is the ratio of the yield of $B \to D^{**}\tau^+\nu_\tau$ decay candidates to the signal decays. This yield is computed assuming that the ratio of the decay rates lies between the ratio of available phase space (0.18) and the predictions of Ref. [47] (0.06) and taking into account the relative efficiencies of the different channels.

(iv) $N^{\rm sv}_{D^0}$ is the yield of $B \to D^{*-}D^0X$ decays where the three pions originate from the same vertex (SV) as the D^0 vertex. The $D^0 \to K^+\pi^-\pi^+\pi^-(\pi^0)$ decays are reconstructed by recovering a charged kaon pointing to the 3π vertex in nonisolated events. The exclusive $D^0 \to K^+\pi^-\pi^+\pi^-$ peak is used to apply a 5% Gaussian constraint to this parameter, accounting for the knowledge of the efficiency in finding the additional kaon.

(v) $f^{v_1v_2}_{D^0}$ is the ratio of $B \to D^{*-}D^0X$ decays where at least one pion originates from the D^0 vertex and the other pion(s) from a different vertex, normalized to $N^{\rm sv}_{D^0}$. This is the case when the soft pion from a D^{*-} decay is reconstructed as it was produced at the 3π vertex.

(vi) f_{D^+} is the ratio of $B \to D^{*-}D^+X$ decays with respect to those containing a D_s^+ meson.

(vii) N_{D_s} is the yield of events involving a D_s^+. The parameters $f_{D_s^+}$, $f_{D_{s0}^{*+}}$, $f_{D_{s1}^+}$, $f_{D_s^+X}$, $f_{(D_s^+X)_s}$ and k, defined in Sec. IV B, are used after correcting for efficiency.

(viii) $N_{B\to D^*3\pi X}$ is the yield of $B \to D^{*-}3\pi X$ events where the three pions come from the B vertex. This value is constrained by using the observed ratio between $B^0 \to D^{*-}3\pi$ exclusive and $B \to D^{*-}3\pi X$ inclusive decays, corrected for efficiency.

(ix) N_{B1B2} is the yield of combinatorial background events where the D^{*-} and the 3π system come from different B decays. Its yield is fixed by using the yield of wrong-sign events $D^{*-}\pi^-\pi^+\pi^-$ in the region $m(D^{*-}\pi^-\pi^+\pi^-) > 5.1$ GeV/c^2.

(x) $N_{{\rm not}D^*}$ is the combinatorial background yield with a fake D^{*-}. Its value is fixed by using the number of events in the $\bar{D}^0$ mass sidebands of the $D^{*-} \to \bar{D}^0\pi^-$ decay.

TABLE V. Summary of fit components and their corresponding normalization parameters. The first three components correspond to parameters related to the signal.

Fit component	Normalization
$B^0 \to D^{*-}\tau^+(\to 3\pi\bar{\nu}_\tau)\nu_\tau$	$N_{\rm sig} \times f_{\tau\to 3\pi\nu}$
$B^0 \to D^{*-}\tau^+(\to 3\pi\pi^0\bar{\nu}_\tau)\nu_\tau$	$N_{\rm sig} \times (1 - f_{\tau\to 3\pi\nu})$
$B \to D^{**}\tau^+\nu_\tau$	$N_{\rm sig} \times f_{D^{**}\tau\nu}$
$B \to D^{*-}D^+X$	$f_{D^+} \times N_{D_s}$
$B \to D^{*-}D^0X$ different vertices	$f^{v_1v_2}_{D^0} \times N^{\rm sv}_{D^0}$
$B \to D^{*-}D^0X$ same vertex	$N^{\rm sv}_{D^0}$
$B^0 \to D^{*-}D_s^+$	$N_{D_s} \times f_{D_s^+}/k$
$B^0 \to D^{*-}D_s^{*+}$	$N_{D_s} \times 1/k$
$B^0 \to D^{*-}D^*_{s0}(2317)^+$	$N_{D_s} \times f_{D^{*+}_{s0}}/k$
$B^0 \to D^{*-}D_{s1}(2460)^+$	$N_{D_s} \times f_{D^+_{s1}}/k$
$B^{0,+} \to D^{**}D_s^+X$	$N_{D_s} \times f_{D_s^+X}/k$
$B_s^0 \to D^{*-}D_s^+X$	$N_{D_s} \times f_{(D_s^+X)_s}/k$
$B \to D^{*-}3\pi X$	$N_{B\to D^*3\pi X}$
B1B2 combinatorics	N_{B1B2}
Combinatoric D^{*-}	$N_{{\rm not}D^*}$

A. Fit results

The results of the three-dimensional fit are shown in Table VI and Fig. 16. A raw number of 1336 decays translates into a yield of $N_{\rm sig} = 1296 \pm 86$ $B^0 \to D^{*-}\tau^+\nu_\tau$ decays, after a correction of -3% due to a fit bias is applied, as detailed below. Figure 17 shows the results of the fit in bins of the BDT output. The two most discriminant variables of the BDT response are the variables $\min[m(\pi^+\pi^-)]$ and $m(D^{*-}3\pi)$. Figure 18 shows the fit results projected onto these variables. A good agreement with data and the post-fit model is found. The fit χ^2 is 1.15 per degree of freedom, after taking into account the statistical fluctuation in the simulation templates, and 1.8

TABLE VI. Fit results for the three-dimensional fit. The constraints on the parameters $f_{D_s^+}$, $f_{D_{s0}^{*+}}$, $f_{D_{s1}^+}$, $f_{D_s^+X}$ and $f_{(D_s^+X)_s}$ are applied taking into account their correlations.

Parameter	Fit result	Constraint
$N_{\rm sig}$	1296 ± 86	
$f_{\tau\to 3\pi\nu}$	0.78	0.78 (fixed)
$f_{D^{**}\tau\nu}$	0.11	0.11 (fixed)
$N_{D^0}^{\rm sv}$	445 ± 22	445 ± 22
$f_{D^0}^{v_1v_2}$	0.41 ± 0.22	
N_{D_s}	6835 ± 166	
f_{D^+}	0.245 ± 0.020	
$N_{B\to D^*3\pi X}$	424 ± 21	443 ± 22
$f_{D_s^+}$	0.494 ± 0.028	0.467 ± 0.032
$f_{D_{s0}^{*+}}$	$0^{+0.010}_{-0.000}$	$0^{+0.042}_{-0.000}$
$f_{D_{s1}^+}$	0.384 ± 0.044	0.444 ± 0.064
$f_{D_s^+X}$	0.836 ± 0.077	0.647 ± 0.107
$f_{(D_s^+X)_s}$	0.159 ± 0.034	0.138 ± 0.040
N_{B1B2}	197	197 (fixed)
$N_{\rm not D^*}$	243	243 (fixed)

without. Due to the limited size of the simulation samples used to build the templates (the need to use templates from inclusive b -hadron decays requires extremely large simulation samples), the existence of empty bins in the templates introduces potential biases in the determination of the signal yield that must be taken into account. To study this effect, a method based on the use of kernel density estimators (KDE) [48] is used. For each simulated sample, a three-dimensional density function is produced. Each KDE is then transformed in a three-dimensional template, where bins that were previously empty may now be filled. These new templates are used to build a smoothed fit model. The fit is repeated with different signal yield hypotheses. The results show that a bias is observed for low values of the generated signal yield that decreases when the generated signal yield increases. For the value found by the nominal fit, a bias of +40 decays is found, and is used to correct the fit result.

The statistical contribution to the total uncertainty is determined by performing a second fit where the parameters governing the templates shapes of the double-charmed decays, $f_{D_s^+}$, $f_{D_{s0}^{*+}}$, $f_{D_{s1}^+}$, $f_{D_s^+X}$, $f_{(D_s^+X)_s}$ and $f_{D^0}^{v_1v_2}$, are fixed to the values obtained in the first fit. The quadratic difference between the uncertainties provided by the two fits is taken as systematic uncertainty due to the knowledge of the $B \to D^{*-}D_s^+X$ and $B \to D^{*-}D^0X$ decay models, and reported in Table VII.

VI. DETERMINATION OF NORMALIZATION YIELD

Figure 7 shows the $D^{*-}3\pi$ mass after the selection of the normalization sample. A clear B^0 signal peak is seen. In order to determine the normalization yield, a fit is performed in the region between 5150 and 5400 MeV$/c^2$. The signal component is described by the sum of a Gaussian function and a Crystal Ball function [49]. An exponential function is used to describe the background. The result of the fit is shown in Fig. 19. The yield obtained is 17808 ± 143.

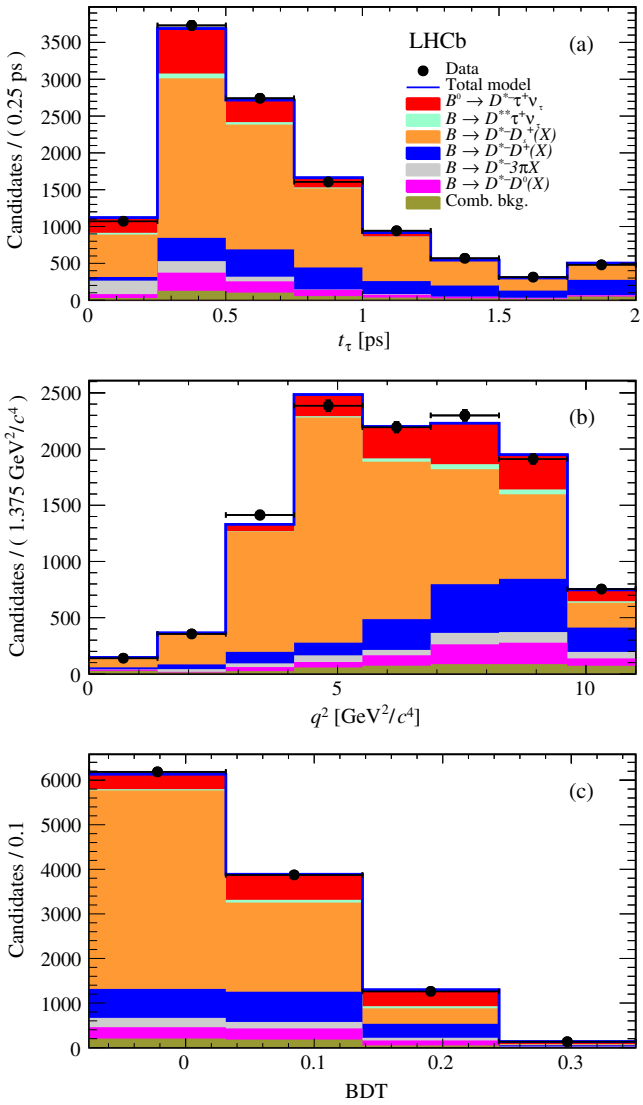

FIG. 16. Projections of the three-dimensional fit on the (a) 3π decay time, (b) q^2 and (c) BDT output distributions. The fit components are described in the legend.

The fit is also performed with alternative configurations, namely with a different fit range or requiring the common mean value of the signal functions to be the same in the 7 and 8 TeV data samples. The maximum differences between signal yields in alternative and nominal configurations are 14 and 62 for the 7 and 8 TeV data samples, respectively, and are used to assign systematic uncertainties to the normalization yields.

Figure 20 shows the $m(3\pi)$ distribution for candidates with $D^{*-}3\pi$ mass between 5200 and 5350 MeV$/c^2$ for the full data sample. The spectrum is dominated by the

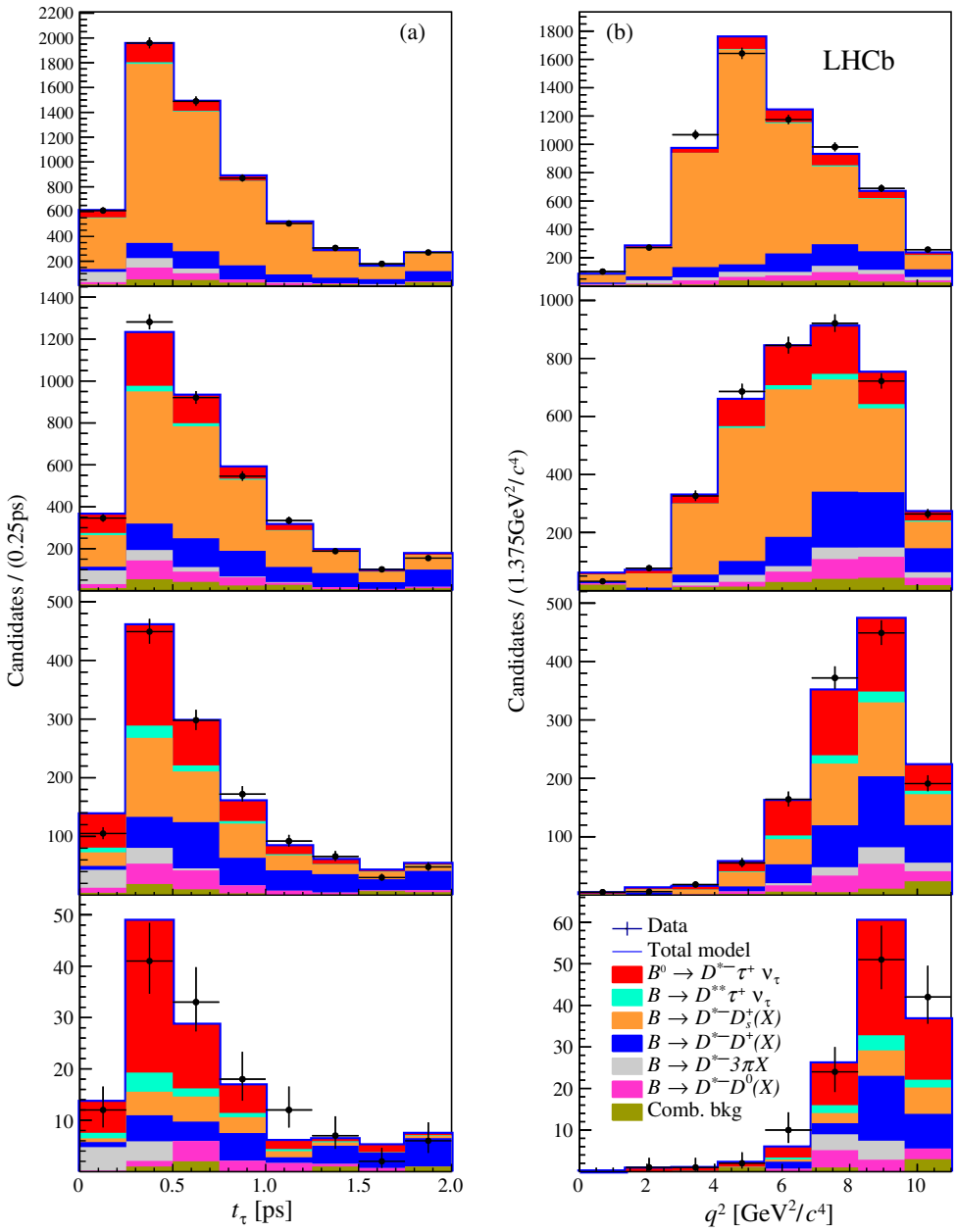

FIG. 17. Distributions of (a) t_τ and (b) q^2 in four different BDT bins, with increasing values of the BDT response from top to bottom. The fit components are described in the legend.

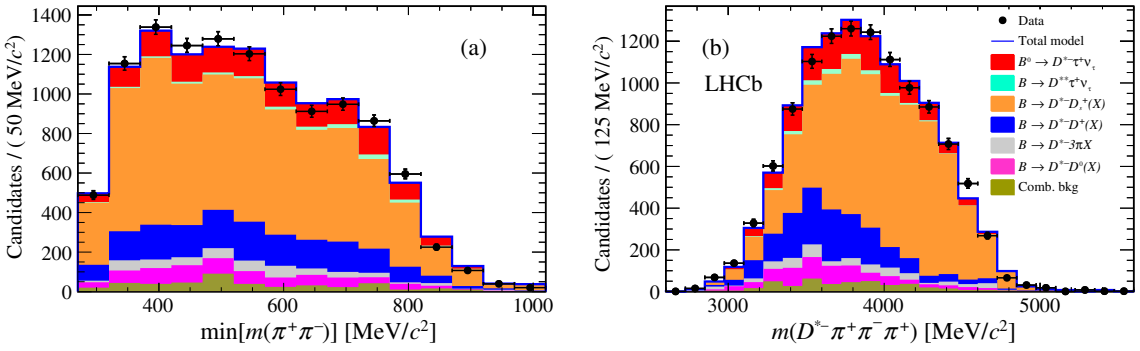

FIG. 18. Projection of the fit results on (a) min$[m(\pi^+\pi^-)]$ and (b) $m(D^{*-}3\pi)$ distributions. The fit components are described in the legend.

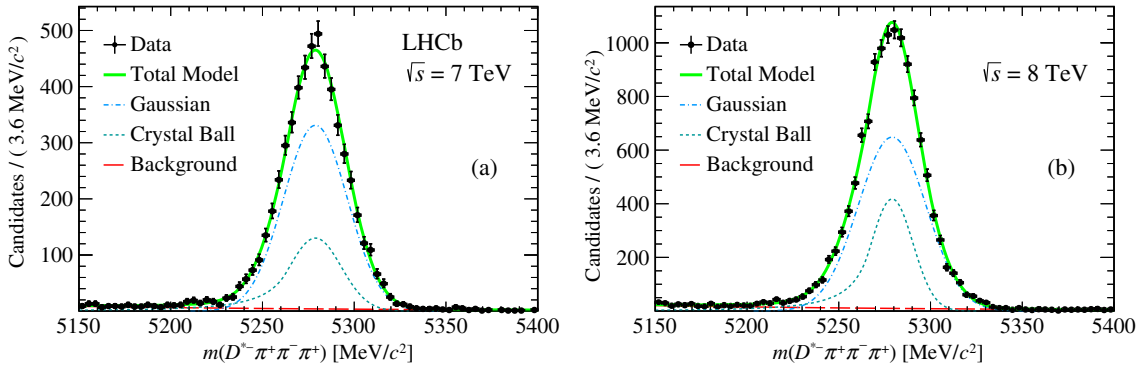

FIG. 19. Fit to the $m(D^{*-}3\pi)$ distribution after the full selection in the (a) $\sqrt{s} = 7$ TeV and (b) 8 TeV data samples.

$a_1(1260)^+$ resonance but also a smaller peak due to the $D_s^+ \to 3\pi$ decay is visible and is subtracted. A fit with the sum of a Gaussian function modeling the D_s^+ mass peak, and an exponential describing the combinatorial background, is performed to estimate this D_s^+ contribution, giving 151 ± 22 candidates. As a result, the number of normalization decays in the full data sample is $N_{\rm norm} = 17\,660 \pm 143({\rm stat}) \pm 64({\rm syst}) \pm 22({\rm sub})$, where the third uncertainty is due to the subtraction of the $B^0 \to D^{*-}D_s^+$ component.

VII. DETERMINATION OF $\mathcal{K}(D^{*-})$

The result

$$\mathcal{K}(D^{*-}) = 1.97 \pm 0.13({\rm stat}) \pm 0.18({\rm syst}),$$

is obtained using Eq. (3). The ratio of efficiencies between the signal and normalization modes, shown in Table II, differs from unity due to the softer momentum spectrum of the signal particles and the correspondingly lower trigger efficiency. The effective sum of the branching fractions for the $\tau^+ \to 3\pi\bar{\nu}_\tau$ and $\tau^+ \to 3\pi\pi^0\bar{\nu}_\tau$ decays is $(13.81 \pm 0.07)\%$ [46]. This includes the 3π mode (without K^0), a very small feed-down from τ five-prong decays, the $3\pi\,\pi^0$ mode (without K^0), and only 50% of the $3\pi\,\pi^0\,\pi^0$ mode due to the smaller efficiency of this decay mode. This latter contribution results in a 1% correction (see Sec. VIII A). Finally, a correction factor 1.056 ± 0.025 is applied when computing $\mathcal{K}(D^{*-})$ in order to account for residual efficiency discrepancies between data and simulation regarding PID and trigger. The event multiplicity, measured by the scintillating-pad detector, affects the efficiency for the fraction of the data sample which is triggered at the hardware trigger level by particles in the event other than those from the $D^{*-}\tau^+\nu_\tau$ candidate. An imperfect description of this multiplicity in the simulation does not cancel completely in $\mathcal{K}(D^{*-})$. The correction factor also includes a small feed-down contribution from $B_s^0 \to D_s^{**-}\tau^+\nu_\tau$ decays, where $D_s^{**-} \to D^{*-}K^0$, that is taken into account according to simulation.

As a further check of the analysis, measurements of $\mathcal{K}(D^{*-})$ are performed in mutually exclusive subsamples, obtained by requiring different trigger conditions and center-of-mass energies. All of these results are found to be compatible with the result obtained with the full sample. Changing the requirement on the minimal BDT output value, as well as the bounds of the nuisance parameters, does not change the final result.

VIII. SYSTEMATIC UNCERTAINTIES

The systematic uncertainties on $\mathcal{K}(D^{*-})$ are subdivided into four categories: the knowledge of the signal model,

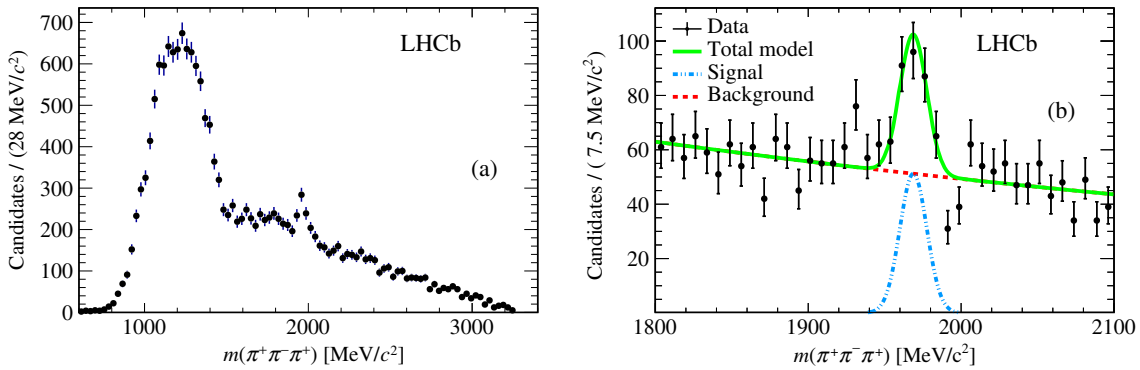

FIG. 20. (a) Distribution of $m(3\pi)$ after selection, requiring $m(D^{*-}3\pi)$ to be between 5200 and 5350 MeV/c^2; (b) fit in the mass region around the D_s^+.

including τ decay models; the modeling of the various background sources; possible biases in the fit procedure due to the limited size of the simulated samples; and trigger selection efficiencies, external inputs and particle identification efficiency. Table VII summarizes the results.

A. Signal model uncertainties

The uncertainty in the relative proportion of signal events in the mode $\tau^+ \to 3\pi\bar{\nu}_\tau$ and $\tau^+ \to 3\pi\pi^0\bar{\nu}_\tau$ affects the fit results. Taking into account the relative efficiencies, an uncertainty of 0.01 is assigned to $f_{\tau\to 3\pi\nu}$. A fit is performed with this fraction constrained to 0.78 ± 0.01 using a Gaussian function. A second fit is done fixing the fraction to the value found by the first fit. The squared difference between the uncertainties of the two fits is taken as the systematic uncertainty due to the signal composition, resulting in a 0.7% systematic uncertainty.

To estimate the systematic uncertainty due to the knowledge of the $B^0 \to D^{*-}\tau^+\nu_\tau$ form factors, a study based on pseudoexperiments is performed. A total of 100 fits to generated samples is done by varying the values of the parameters $R_1(1)$, $R_2(1)$ and ρ^2 of Ref. [2] which govern the fraction of each spin configuration in the form-factor templates. The parameters are varied according to a multivariate Gaussian distribution using their uncertainties and correlations. The parameter $R_0(1) = 1.14 \pm 0.11$ is varied under the conservative assumption that it is not correlated with the other parameters. A systematic uncertainty of 0.7% on the signal yield is obtained by taking the standard deviation of the distribution of the fitted signal yields.

A value of 1% systematic uncertainty of the efficiency due to the form factor reweighting is computed by repeating the fit without it.

The effect of the τ polarization is studied separately for $\tau^+ \to 3\pi\bar{\nu}_\tau$ and $\tau^+ \to 3\pi\pi^0\bar{\nu}_\tau$ decays. Due to the $a_1(1260)^+$ dominance observed in the $\tau^+ \to 3\pi\bar{\nu}_\tau$ decay, the sensitivity of the 3π momenta to the polarization is negligible and therefore no systematic uncertainty is assigned due to this effect. For the $\tau^+ \to 3\pi\pi^0\bar{\nu}_\tau$ decay mode, the signal is simulated in two configurations: using either the TAUOLA [50] model or a pure phase-space model. The effect of the τ polarization is evaluated by multiplying the efficiency by the ratio of the distributions of the cosine of α (the angle between the 3π momentum in the τ rest frame and the τ direction in the laboratory frame) generated with the two configurations. This produces a relative change in the efficiency of 1.5%. This value, scaled by the relative fraction of the $\tau^+ \to 3\pi\pi^0\bar{\nu}_\tau$ component with respect to the total, gives a systematic uncertainty of 0.4%.

Other τ decays could contribute to the signal yield. They are either decays with three charged tracks in the final states ($K^+\pi^-\,\pi^+$, $K^+K^-\pi^+$, $\pi^+\,\pi^-\,\pi^+\,\pi^0\,\pi^0$) or five charged tracks, all of them having very small branching fractions compared to the $\tau^+ \to 3\pi(\pi^0)\bar{\nu}_\tau$ decay mode. The study of a dedicated simulation sample with inclusive τ decays indicates an effect of 1% that is taken as a systematic uncertainty.

The $B \to D^{**}\tau\nu_\tau$ fraction used for the nominal fit, 0.11, is assigned a 40% uncertainty, based on the results of an auxiliary study of $B^- \to D_1(2420)^0\tau^+\nu_\tau$ decays, where $D_1(2420)^0 \to D^{*-}\pi^+$. These results give a systematic uncertainty on the signal yield of 2.3%.

An additional systematic uncertainty of 1.5% due to the feed-down from $B_s^0 \to D_s^{**}\tau^+\nu_\tau$ decays is assigned, under the assumption that the yield of these decays in the simulation has an uncertainty of 50%, determined to be the upper limit from a study performed on simulated data.

B. Background-related systematic uncertainties

This section lists the systematic uncertainties due to the modeling of different background sources, such as the D_s^+ decay model, double-charm and combinatorial contributions.

Candidates in the low BDT output region are used to correct the composition of D_s^+ decays in simulation. From the fit to this data sample corrections are obtained, which are used to generate 1000 alternative D_s^+ templates for each D_s^+ component in the nominal three-dimensional fit. Each alternative template is produced by varying the nominal template accounting for the uncertainty and correlations between the D_s^+ subcomponents according to a Gaussian distribution. These alternative templates are employed to refit the model to the data. The difference between the signal yield of the alternative and the nominal fits, divided by the yield of the nominal fit, is fitted with a Gaussian function and a systematic uncertainty of 2.5% is determined.

The mass variables that are expected to be significantly correlated with the fit variables q^2 and BDT, are $m(D^{*-}3\pi)$, $m(3\pi)$, $\min[m(\pi^+\pi^-)]$, $\max[m(\pi^+\pi^-)]$ and $m(\pi^+\pi^+)$.[4] The corresponding effect on the fit result of these variables is empirically studied by varying the distributions using a quadratic interpolation method: for each template, two alternative templates are produced, with a variation of $\pm 1\sigma$. Then, the fit enables the interpolation between the nominal and the alternative templates to be made with a linear weight. Each nuisance parameter is allowed to float in the range $[-1, +1]$ and a loose Gaussian constraint with $\sigma = 1$ is included. This method is used to compute systematic uncertainties due to the knowledge of the shape of the templates. The corresponding systematic uncertainty is 2.9%. A systematic uncertainty of 2.6% arises due to the composition of the $B \to D^{*-}D_s^+(X)$ and $B \to D^{*-}D^0(X)$ decays, as discussed in Sec. IV. The use of the D_s^+ exclusive

[4]Only $m(D^{*-}3\pi)$ is considered for the $D^{*-}D_s^+$ case, since the effect of the other three variables is included in the systematic uncertainty due to the D_s^+ decay model.

reconstruction in 3π helps to limit the size of this uncertainty.

The systematic uncertainty due to the knowledge of the shape of the residual prompt background component is estimated by applying the same interpolation technique to the corresponding template. When combined with the knowledge of the normalization of this background, this gives an overall uncertainty of 2.8%.

The same method is again used to assess the systematic uncertainty due to the shape of the combinatorial background. The change in the signal yield provides a systematic uncertainty of 0.7%.

Another systematic uncertainty is due to the normalization of this background. This uncertainty is computed by performing the fit with a 30% Gaussian constraint around the nominal value. The resulting difference with respect to the nominal fit is 0.1%, which is assigned as systematic uncertainty. This uncertainty has a negligible effect on the total systematic uncertainty associated with the shape of the combinatorial background.

C. Fit-related systematic uncertainties

To assess the systematic uncertainty relative to the bias due to empty bins in the templates used in the fit, the study performed using the KDE method is repeated implementing different smoothing parameters. A difference in the signal yield of 1.3% is assigned as the systematic uncertainty due to the bias observed in the fit.

In order to estimate the systematic uncertainty due to the limited size of the simulated samples, a bootstrap method is used. Each template from the nominal model is used to produce new templates sampled from the originals by using a bootstrap procedure based on random selection with replacement, varied bin-by-bin according to a Poisson distribution. This procedure is repeated 500 times. A Gaussian fit to the distributions of signal yields provides a 4.1% effect taken as the systematic uncertainty due to the limited size of the simulated samples.

D. Uncertainties related to the selection

In this section systematic uncertainties related to the selection criteria are discussed. Such uncertainties stem from the choice of the trigger strategy, the online and offline selection of the candidates, the normalization and external inputs, and the efficiency of the PID criteria.

The trigger efficiency is studied on data using the fraction of the events where the trigger was fired by particles other than the six tracks forming the signal candidate, as a function of the two most important variables in this analysis, t_τ and $m(D^{*-}3\pi)$, the latter being highly correlated with q^2. Corrections on the t_τ and $m(D^{*-}3\pi)$ distributions due to different trigger efficiency between data and simulation are applied. This gives a change in the number of signal candidates of 1.0% for the t_τ and 0.7% for the $m(D^{*-}3\pi)$ corrections. The sum in quadrature of these two contributions, taken as systematic uncertainty related to the trigger efficiency, is 1.2%.

An additional 1% systematic uncertainty arises from a mismatch between data and simulation in the occupancy of the event.

The relative efficiency between the signal and the normalization channels is precisely determined from simulated samples. Discrepancies between data and simulation, due to online and offline selection criteria, introduce a 2% of systematic uncertainty for both.

A 1% systematic uncertainty is assigned on the charged isolation criterion, due to differences observed between the $B^0 \to D^{*-}\tau^+\nu_\tau$ and the $B^0 \to D^{*-}3\pi$ simulations.

All selection criteria, except the detached-vertex topology requirement, are common to the signal and normalization decays. The corresponding efficiencies are therefore directly determined from data by fitting the number of events in the $B^0 \to D^{*-}3\pi$ mass peak before and after each selection, and no systematic uncertainty is assigned. To compute the systematic uncertainty attributed to the knowledge of the relative efficiencies corresponding to the different signal and normalization vertex topologies, the vertex position uncertainty distribution is split into three regions: between -4σ and -2σ, between -2σ and 2σ and between 2σ and 4σ, where σ is the reconstructed uncertainty on the distance along the beam line of the B^0 and 3π vertices. Then a ratio between the number of candidates in the outer regions and the number of candidates in the inner region is computed for the candidates which have $m(D^{*-}3\pi)$ in the exclusive $B^0 \to D^{*-}3\pi$ peak. The same procedure is performed for the candidates outside the $B^0 \to D^{*-}3\pi$ peak, which exhibit a signal-like behavior. The procedure is repeated for data, and the ratio between data and simulation gives rise to a 2% systematic uncertainty.

The simulation is corrected in order to match the performance of PID criteria measured in data. Correction factors are applied in bins of momentum, pseudorapidity and global event multiplicity, after having adjusted the simulated event multiplicity to that observed using real data. To assess the systematic uncertainty due to the choice of the binning scheme used to correct simulation, two new schemes are derived from the default with half and twice the number of bins, the default configuration consisting of fifteen bins in momentum, seven in pseudorapidity and three in the global event multiplicity. The correction procedure is repeated with these two alternate schemes, leading to a systematic uncertainty related to PID of 1.3%.

The normalization channel consists of exactly the same final state as the signal. In this way, differences between data and simulation are minimized. The systematic uncertainty in the normalization yield is determined to be equal to 1%. The statistical uncertainty attributed to the normalization yield is included in the statistical uncertainty quoted for each result in this paper. Differences between data and simulation in the modeling of the $B^0 \to D^{*-}3\pi$ decay

TABLE VII. List of the individual systematic uncertainties for the measurement of the ratio $\mathcal{B}(B^0 \to D^{*-}\tau^+\nu_\tau)/\mathcal{B}(B^0 \to D^{*-}3\pi)$.

Contribution	Value in %
$\mathcal{B}(\tau^+ \to 3\pi\bar{\nu}_\tau)/\mathcal{B}(\tau^+ \to 3\pi(\pi^0)\bar{\nu}_\tau)$	0.7
Form factors (template shapes)	0.7
Form factors (efficiency)	1.0
τ polarization effects	0.4
Other τ decays	1.0
$B \to D^{**}\tau^+\nu_\tau$	2.3
$B_s^0 \to D_s^{**}\tau^+\nu_\tau$ feed-down	1.5
$D_s^+ \to 3\pi X$ decay model	2.5
D_s^+, D^0 and D^+ template shape	2.9
$B \to D^{*-}D_s^+(X)$ and $B \to D^{*-}D^0(X)$ decay model	2.6
$D^{*-}3\pi X$ from B decays	2.8
Combinatorial background (shape + normalization)	0.7
Bias due to empty bins in templates	1.3
Size of simulation samples	4.1
Trigger acceptance	1.2
Trigger efficiency	1.0
Online selection	2.0
Offline selection	2.0
Charged-isolation algorithm	1.0
Particle identification	1.3
Normalization channel	1.0
Signal efficiencies (size of simulation samples)	1.7
Normalization channel efficiency (size of simulation samples)	1.6
Normalization channel efficiency (modeling of $B^0 \to D^{*-}3\pi$)	2.0
Total uncertainty	9.1

impact the efficiency of the normalization channel and result in a 2.0% systematic uncertainty on $\mathcal{K}(D^{*-})$.

The branching fraction for the normalization channel, obtained by averaging the measurements of Refs. [22–24], has an uncertainty of 3.9%. A 2.0% uncertainty arising from the knowledge of the $B^0 \to D^{*-}\mu^+\nu_\mu$ branching fraction is added in quadrature to obtain a 4.5% total uncertainty on $\mathcal{R}(D^{*-})$ due to external inputs.

E. Summary of systematic uncertainties

Table VII summarizes the systematic uncertainties on the measurement of the ratio $\mathcal{B}(B^0 \to D^{*-}\tau^+\nu_\tau)/\mathcal{B}(B^0 \to D^{*-}3\pi)$. The total uncertainty is 9.1%. For $\mathcal{R}(D^{*-})$, a 4.5% systematic uncertainty due to the knowledge of the external branching fractions is added.

IX. CONCLUSION

In conclusion, the ratio of branching fractions between the $B^0 \to D^{*-}\tau^+\nu_\tau$ and the $B^0 \to D^{*-}3\pi$ decays is measured to be

$$\mathcal{K}(D^{*-}) = 1.97 \pm 0.13(\text{stat}) \pm 0.18(\text{syst}),$$

where the first uncertainty is statistical and the second systematic. Using the branching fraction $\mathcal{B}(B^0 \to D^{*-}3\pi) = (7.214 \pm 0.28) \times 10^{-3}$ from the weighted average of the measurements by the LHCb [22], *BABAR* [23], and Belle [24] Collaborations, a value of the absolute branching fraction of the $B^0 \to D^{*-}\tau^+\nu_\tau$ decay is obtained

$$\mathcal{B}(B^0 \to D^{*-}\tau^+\nu_\tau) = (1.42 \pm 0.094(\text{stat}) \pm 0.129(\text{syst}) \pm 0.054(\text{ext})) \times 10^{-2},$$

where the third uncertainty originates from the limited knowledge of the branching fraction of the normalization mode. The precision of this measurement is comparable to that of the current world average of Ref. [46]. The first determination of $\mathcal{R}(D^{*-})$ performed by using three-prong τ decays is obtained by using the measured branching fraction of $\mathcal{B}(B^0 \to D^{*-}\mu^+\nu_\mu) = (4.88 \pm 0.10) \times 10^{-2}$ from Ref. [20]. The result

$$\mathcal{R}(D^{*-}) = 0.291 \pm 0.019(\text{stat}) \pm 0.026(\text{syst}) \pm 0.013(\text{ext})$$

is one of the most precise single measurements performed so far. It is 1.1 standard deviations higher than the SM prediction (0.252 ± 0.003) of Ref. [2] and consistent with previous determinations. This R(D^*) measurement, being proportional to $\mathcal{B}(B^0 \to D^{*-}3\pi)$ and inversely proportional to $\mathcal{B}(B^0 \to D^{*-}\mu^+\nu_\mu)$, will need to be rescaled accordingly when more precise values of these inputs are made available in the future. An average of this measurement with the LHCb result using $\tau^+ \to \mu^+\nu_\mu\bar{\nu}_\tau$ decays [17], accounting for small correlations due to form factors, τ polarization and $D^{**}\tau^+\nu_\tau$ feed-down, gives a value of $\mathcal{R}(D^{*-}) = 0.310 \pm 0.0155(\text{stat}) \pm 0.0219(\text{syst})$, consistent with the world average and 2.2 standard deviations above the SM prediction. The overall status of $\mathcal{R}(D)$ and $\mathcal{R}(D^*)$ measurements is reported in Ref. [20]. After inclusion of this result, the combined discrepancy of $\mathcal{R}(D)$ and $\mathcal{R}(D^*)$ determinations with the SM prediction is 4.1σ.

The novel technique presented in this paper, allowing the reconstruction and selection of semitauonic decays with $\tau^+ \to 3\pi(\pi^0)\bar{\nu}_\tau$ transitions, can be applied to all the other semitauonic decays, such as those of B^+, B_s^0, B_c^+ and Λ_b^0. This technique also allows isolation of large signal samples with high purity, which can be used to measure angular distributions and other observables proposed in the literature to discriminate between SM and new physics contributions. The inclusion of further data collected by LHCb at $\sqrt{s} = 13$ TeV will result in an overall uncertainty on $\mathcal{R}(D^{*-})$ using this technique comparable to that of the current world average.

ACKNOWLEDGMENTS

We express our gratitude to our colleagues in the CERN accelerator departments for the excellent performance of the LHC. We thank the technical and administrative staff at the LHCb institutes. We acknowledge support from CERN and from the national agencies: CAPES, CNPq, FAPERJ and FINEP (Brazil); MOST and NSFC (China); CNRS/IN2P3 (France); BMBF, DFG and MPG (Germany); INFN (Italy); NWO (The Netherlands); MNiSW and NCN (Poland); MEN/IFA (Romania); MinES and FASO (Russia); MinECo (Spain); SNSF and SER (Switzerland); NASU (Ukraine); STFC (United Kingdom); NSF (U.S.). We acknowledge the computing resources that are provided by CERN, IN2P3 (France), KIT and DESY (Germany), INFN (Italy), SURF (The Netherlands), PIC (Spain), GridPP (United Kingdom), RRCKI and Yandex LLC (Russia), CSCS (Switzerland), IFIN-HH (Romania), CBPF (Brazil), PL-GRID (Poland) and OSC (U.S.). We are indebted to the communities behind the multiple open-source software packages on which we depend. Individual groups or members have received support from AvH Foundation (Germany), EPLANET, Marie Skłodowska-Curie Actions and ERC (European Union), ANR, Labex P2IO, ENIGMASS and OCEVU, and Région Auvergne-Rhône-Alpes (France), RFBR and Yandex LLC (Russia), GVA, XuntaGal and GENCAT (Spain), Herchel Smith Fund, the Royal Society, the English-Speaking Union and the Leverhulme Trust (United Kingdom).

[1] S. Schael *et al.* (ALEPH Collaboration, DELPHI Collaboration, L3 Collaboration, OPAL Collaboration, LEP Electroweak Working Group Collaboration), Electroweak measurements in electron-positron collisions at W-boson-pair energies at LEP, Phys. Rep. **532**, 119 (2013).

[2] S. Fajfer, J. F. Kamenik, and I. Nišandžić, On the $B \to D^* \tau \bar{\nu}_\tau$ sensitivity to new physics, Phys. Rev. D **85**, 094025 (2012).

[3] D. Bigi and P. Gambino, Revisiting $B \to D \ell \nu$, Phys. Rev. D **94**, 094008 (2016).

[4] F. U. Bernlochner, Z. Ligeti, M. Papucci, and D. J. Robinson, Combined analysis of semileptonic B decays to D and D^*: $R(D^{(*)})$, $|V_{cb}|$, and new physics, Phys. Rev. D **95**, 115008 (2017).

[5] S. Jaiswal, S. Nandi, and S. K. Patra, Extraction of $|V_{cb}|$ from $B \to D^{(*)} \ell \nu_\ell$ and the Standard Model predictions of $R(D^{(*)})$, J. High Energy Phys. 12 (2017) 060.

[6] D. Bigi, P. Gambino, and S. Schacht, $R(D^*)$, $|V_{cb}|$, and the heavy quark symmetry relations between form factors, J. High Energy Phys. 11 (2017) 061.

[7] M. Tanaka, Charged Higgs effects on exclusive semitauonic B decays, Z. Phys. C **67**, 321 (1995).

[8] W. Buchmüller, R. Rückl, and D. Wyler, Leptoquarks in lepton quark collisions, Phys. Lett. B **191**, 442 (1987); Erratum, Phys. Lett. B**448**, 320E (1999).

[9] S. Davidson, D. C. Bailey, and B. A. Campbell, Model independent constraints on leptoquarks from rare processes, Z. Phys. C **61**, 613 (1994).

[10] A. Greljo, G. Isidori, and D. Marzocca, On the breaking of lepton flavor universality in B decays, J. High Energy Phys. 07 (2015) 142.

[11] S. M. Boucenna, A. Celis, J. Fuentes-Martín, A. Vicente, and J. Virto, Phenomenology of an $\mathrm{SU}(2) \times \mathrm{SU}(2) \times \mathrm{U}(1)$ model with lepton-flavour non-universality, J. High Energy Phys. 12 (2016) 59.

[12] B. Bhattacharya, A. Datta, J.-P. Guévin, D. London, and R. Watanabe, Simultaneous explanation of the R_K and $R(D^{(*)})$ puzzles: A model analysis, J. High Energy Phys. 1 (2017) 15.

[13] J. P. Lees *et al.* (*BABAR* Collaboration), Evidence for an Excess of $\bar{B} \to D^* \tau^- \bar{\nu}_\tau$ Decays, Phys. Rev. Lett. **109**, 101802 (2012).

[14] J. P. Lees *et al.* (*BABAR* Collaboration), Measurement of an excess of $\bar{B} \to D^{(*)} \tau^- \bar{\nu}_\tau$ decays and implications for charged Higgs bosons, Phys. Rev. D **88**, 072012 (2013).

[15] M. Huschle *et al.* (Belle Collaboration), Measurement of the branching ratio of $\bar{B} \to D^{(*)} \tau^- \bar{\nu}_\tau$ relative to $\bar{B} \to D^{(*)} \ell^- \bar{\nu}_\ell$ decays with hadronic tagging at Belle, Phys. Rev. D **92**, 072014 (2015).

[16] Y. Sato *et al.* (Belle Collaboration), Measurement of the branching ratio of $\bar{B}^0 \to D^{*+} \tau^- \bar{\nu}_\tau$ relative to $\bar{B}^0 \to D^{*+} \ell^- \bar{\nu}_\ell$ decays with a semileptonic tagging method, Phys. Rev. D **94**, 072007 (2016).

[17] R. Aaij *et al.* (LHCb Collaboration), Measurement of the Ratio of Branching Fractions $\mathcal{B}(\bar{B}^0 \to D^{*+} \tau^- \bar{\nu}_\tau)/\mathcal{B}(\bar{B}^0 \to D^{*+} \mu^- \bar{\nu}_\mu)$, Phys. Rev. Lett. **115**, 111803 (2015).

[18] S. Hirose *et al.* (Belle Collaboration), Measurement of the τ Lepton Polarization and $R(D^*)$ in the Decay $\bar{B} \to D^* \tau^- \bar{\nu}_\tau$, Phys. Rev. Lett. **118**, 211801 (2017).

[19] S. Hirose *et al.* (Belle Collaboration), Measurement of the τ lepton polarization and $R(D^*)$ in the decay $\bar{B} \to D^* \tau^- \bar{\nu}_\tau$ with one-prong hadronic τ decays at Belle, Phys. Rev. D **97**, 012004 (2018).

[20] Y. Amhis *et al.* (Heavy Flavor Averaging Group Collaboration), Averages of b-hadron, c-hadron, and τ-lepton properties as of summer 2016, Eur. Phys. J. C **77**, 895 (2017).

[21] R. Aaij *et al.* (LHCb Collaboration), Measurement of the Ratio of the $B^0 \to D^{*-} \tau^+ \nu_\tau$ and $B^0 \to D^{*-} \mu^+ \nu_\mu$ Branching Fractions Using Three-Prong τ-Lepton Decays, Phys. Rev. Lett. **120**, 171802 (2018).

[22] R. Aaij *et al.* (LHCb Collaboration), Study of $B^0 \to D^{*-} \pi^+ \pi^- \pi^+$ and $B^0 \to D^{*-} K^+ \pi^- \pi^+$ decays, Phys. Rev. D **87**, 092001 (2013).

[23] J. P. Lees *et al.* (*BABAR* Collaboration), Measurement of the $B^0 \to D^{*-} \pi^+ \pi^- \pi^+$ branching fraction, Phys. Rev. D **94**, 091101 (2016).

[24] G. Majumder *et al.* (Belle Collaboration), Observation of $B^0 \to D^{*-}(5\pi)^+$, $B^+ \to D^{*-}(4\pi)^{++}$ and $B^+ \to \bar{D}^{*0}(5\pi)^+$, Phys. Rev. D **70**, 111103 (2004).

[25] A. A. Alves Jr. *et al.* (LHCb Collaboration), The LHCb detector at the LHC, J. Instrum. **3**, S08005 (2008).

[26] R. Aaij *et al.* (LHCb Collaboration), LHCb detector performance, Int. J. Mod. Phys. A **30**, 1530022 (2015).

[27] R. Aaij *et al.*, Performance of the LHCb Vertex Locator, J. Instrum. **9**, P09007 (2014).

[28] R. Arink *et al.*, Performance of the LHCb Outer Tracker, J. Instrum. **9**, P01002 (2014).

[29] M. Adinolfi *et al.*, Performance of the LHCb RICH detector at the LHC, Eur. Phys. J. C **73**, 2431 (2013).

[30] A. A. Alves Jr. *et al.*, Performance of the LHCb muon system, J. Instrum. **8**, P02022 (2013).

[31] T. Sjöstrand, S. Mrenna, and P. Skands, PYTHIA 6.4 physics and manual, J. High Energy Phys. 05 (2006) 026; A brief introduction to PYTHIA 8.1, Comput. Phys. Commun. **178**, 852 (2008).

[32] I. Belyaev *et al.*, Handling of the generation of primary events in Gauss, the LHCb simulation framework, J. Phys. Conf. Ser. **331**, 032047 (2011).

[33] D. J. Lange, The EvtGen particle decay simulation package, Nucl. Instrum. Methods Phys. Res., Sect. A **462**, 152 (2001).

[34] P. Golonka and Z. Was, PHOTOS Monte Carlo: A precision tool for QED corrections in Z and W decays, Eur. Phys. J. C **45**, 97 (2006).

[35] N. Davidson, G. Nanava, T. Przedziński, E. Richter-Wąs, and Z. Wąs, Universal interface of TAUOLA technical and physics documentation, Comput. Phys. Commun. **183**, 821 (2012).

[36] I. M. Nugent, T. Przedziński, P. Roig, O. Shekhovtsova, and Z. Wąs, Resonance chiral Lagrangian currents and experimental data for $\tau^- \to \pi^-\pi^-\pi^+\nu_\tau$, Phys. Rev. D **88**, 093012 (2013).

[37] I. M. Nugent, Invariant mass spectra of $\tau^- \to h^-h^-h^+\nu_\tau$ decays, Nucl. Phys. B, Proc. Suppl. **253–255**, 38 (2014).

[38] J. Allison *et al.* (Geant4 Collaboration), Geant4 developments and applications, IEEE Trans. Nucl. Sci. **53**, 270 (2006); S. Agostinelli *et al.* (Geant4 Collaboration), Geant4: A simulation toolkit, Nucl. Instrum. Methods Phys. Res., Sect. A **506**, 250 (2003).

[39] M. Clemencic, G. Corti, S. Easo, C. R. Jones, S. Miglioranzi, M. Pappagallo, and P. Robbe, The LHCb simulation application, Gauss: Design, evolution and experience, J. Phys. Conf. Ser. **331**, 032023 (2011).

[40] I. Caprini, L. Lellouch, and M. Neubert, Dispersive bounds on the shape of $\bar{B} \to D^*\ell\bar{\nu}$ form-factors, Nucl. Phys. **B530**, 153 (1998).

[41] J. G. Körner and G. A. Schuler, Exclusive semileptonic heavy meson decays including lepton mass effects, Z. Phys. C **46**, 93 (1990).

[42] R. Aaij *et al.*, The LHCb trigger and its performance in 2011, J. Instrum. **8**, P04022 (2013).

[43] V. V. Gligorov and M. Williams, Efficient, reliable and fast high-level triggering using a bonsai boosted decision tree, J. Instrum. **8**, P02013 (2013).

[44] L. Breiman, J. H. Friedman, R. A. Olshen, and C. J. Stone, *Classification and Regression Trees* (Wadsworth International Group, Belmont, California, 1984).

[45] Y. Freund and R. E. Schapire, A decision-theoretic generalization of on-line learning and an application to boosting, J. Comput. Syst. Sci. **55**, 119 (1997).

[46] C. Patrignani *et al.* (Particle Data Group Collaboration), Review of particle physics, Chin. Phys. C **40**, 100001 (2016) and 2017 update.

[47] F. U. Bernlochner and Z. Ligeti, Semileptonic $B_{(s)}$ decays to excited charmed mesons with e, μ, τ and searching for new physics with $R(D^{**})$, Phys. Rev. D **95**, 014022 (2017).

[48] K. S. Cranmer, Kernel estimation in high-energy physics, Comput. Phys. Commun. **136**, 198 (2001).

[49] T. Skwarnicki, Ph.D. thesis, Institute of Nuclear Physics, Krakow, 1986, Report No. DESY-F31-86-02.

[50] Z. Was, TAUOLA for simulation of tau decay and production: Perspectives for precision low energy and LHC applications, Nucl. Phys. B, Proc. Suppl. **218**, 249 (2011).

R. Aaij,[40] B. Adeva,[39] M. Adinolfi,[48] Z. Ajaltouni,[5] S. Akar,[59] J. Albrecht,[10] F. Alessio,[40] M. Alexander,[53] A. Alfonso Albero,[38] S. Ali,[43] G. Alkhazov,[31] P. Alvarez Cartelle,[55] A. A. Alves Jr.,[59] S. Amato,[2] S. Amerio,[23] Y. Amhis,[7] L. An,[3] L. Anderlini,[18] G. Andreassi,[41] M. Andreotti,[17,g] J. E. Andrews,[60] R. B. Appleby,[56] F. Archilli,[43] P. d'Argent,[12] J. Arnau Romeu,[6] A. Artamonov,[37] M. Artuso,[61] E. Aslanides,[6] G. Auriemma,[26] M. Baalouch,[5] I. Babuschkin,[56] S. Bachmann,[12] J. J. Back,[50] A. Badalov,[38,m] C. Baesso,[62] S. Baker,[55] V. Balagura,[7,b] W. Baldini,[17] A. Baranov,[35] R. J. Barlow,[56] C. Barschel,[40] S. Barsuk,[7] W. Barter,[56] F. Baryshnikov,[32] V. Batozskaya,[29] V. Battista,[41] A. Bay,[41] L. Beaucourt,[4] J. Beddow,[53] F. Bedeschi,[24] I. Bediaga,[1] A. Beiter,[61] L. J. Bel,[43] N. Beliy,[63] V. Bellee,[41] N. Belloli,[21,i] K. Belous,[37] I. Belyaev,[32] E. Ben-Haim,[8] G. Bencivenni,[19] S. Benson,[43] S. Beranek,[9] A. Berezhnoy,[33] R. Bernet,[42] D. Berninghoff,[12] E. Bertholet,[8] A. Bertolin,[23] C. Betancourt,[42] F. Betti,[15] M.-O. Bettler,[40] M. van Beuzekom,[43] Ia. Bezshyiko,[42] S. Bifani,[47] P. Billoir,[8] A. Birnkraut,[10] A. Bitadze,[56] A. Bizzeti,[18,u] M. Bjørn,[57] T. Blake,[50] F. Blanc,[41] J. Blouw,[11,†] S. Blusk,[61] V. Bocci,[26] T. Boettcher,[58] A. Bondar,[36,w] N. Bondar,[31] W. Bonivento,[16] I. Bordyuzhin,[32] A. Borgheresi,[21,i] S. Borghi,[56] M. Borisyak,[35] M. Borsato,[39] F. Bossu,[7] M. Boubdir,[9] T. J. V. Bowcock,[54] E. Bowen,[42] C. Bozzi,[17,40] S. Braun,[12] T. Britton,[61] J. Brodzicka,[27] D. Brundu,[16] E. Buchanan,[48] C. Burr,[56] A. Bursche,[16,f] J. Buytaert,[40]

W. Byczynski,[40] S. Cadeddu,[16] H. Cai,[64] R. Calabrese,[17,g] R. Calladine,[47] M. Calvi,[21,i] M. Calvo Gomez,[38,m] A. Camboni,[38,m] P. Campana,[19] D. H. Campora Perez,[40] L. Capriotti,[56] A. Carbone,[15,e] G. Carboni,[25,j] R. Cardinale,[20,h] A. Cardini,[16] P. Carniti,[21,i] L. Carson,[52] K. Carvalho Akiba,[2] G. Casse,[54] L. Cassina,[21] L. Castillo Garcia,[41] M. Cattaneo,[40] G. Cavallero,[20,40,h] R. Cenci,[24,t] D. Chamont,[7] M. G. Chapman,[48] M. Charles,[8] Ph. Charpentier,[40] G. Chatzikonstantinidis,[47] M. Chefdeville,[4] S. Chen,[56] S. F. Cheung,[57] S.-G. Chitic,[40] V. Chobanova,[39] M. Chrzaszcz,[42,27] A. Chubykin,[31] P. Ciambrone,[19] X. Cid Vidal,[39] G. Ciezarek,[43] P. E. L. Clarke,[52] M. Clemencic,[40] H. V. Cliff,[49] J. Closier,[40] V. Coco,[59] J. Cogan,[6] E. Cogneras,[5] V. Cogoni,[16,f] L. Cojocariu,[30] P. Collins,[40] T. Colombo,[40] A. Comerma-Montells,[12] A. Contu,[40] A. Cook,[48] G. Coombs,[40] S. Coquereau,[38] G. Corti,[40] M. Corvo,[17,g] C. M. Costa Sobral,[50] B. Couturier,[40] G. A. Cowan,[52] D. C. Craik,[52] A. Crocombe,[50] M. Cruz Torres,[62] R. Currie,[52] C. D'Ambrosio,[40] F. Da Cunha Marinho,[2] E. Dall'Occo,[43] J. Dalseno,[48] A. Davis,[3] O. De Aguiar Francisco,[54] K. De Bruyn,[6] S. De Capua,[56] M. De Cian,[12] J. M. De Miranda,[1] L. De Paula,[2] M. De Serio,[14,d] P. De Simone,[19] C. T. Dean,[53] D. Decamp,[4] L. Del Buono,[8] H.-P. Dembinski,[11] M. Demmer,[10] A. Dendek,[28] D. Derkach,[35] O. Deschamps,[5] F. Dettori,[54] B. Dey,[65] A. Di Canto,[40] P. Di Nezza,[19] H. Dijkstra,[40] F. Dordei,[40] M. Dorigo,[40] A. Dosil Suárez,[39] L. Douglas,[53] A. Dovbnya,[45] K. Dreimanis,[54] L. Dufour,[43] G. Dujany,[8] K. Dungs,[40] P. Durante,[40] R. Dzhelyadin,[37] M. Dziewiecki,[12] A. Dziurda,[40] A. Dzyuba,[31] N. Déléage,[4] S. Easo,[51] M. Ebert,[52] U. Egede,[55] V. Egorychev,[32] S. Eidelman,[36,w] S. Eisenhardt,[52] U. Eitschberger,[10] R. Ekelhof,[10] L. Eklund,[53] S. Ely,[61] S. Esen,[12] H. M. Evans,[49] T. Evans,[57] A. Falabella,[15] N. Farley,[47] S. Farry,[54] R. Fay,[54] D. Fazzini,[21,i] L. Federici,[25] D. Ferguson,[52] G. Fernandez,[38] P. Fernandez Declara,[40] A. Fernandez Prieto,[39] F. Ferrari,[15] F. Ferreira Rodrigues,[2] M. Ferro-Luzzi,[40] S. Filippov,[34] R. A. Fini,[14] M. Fiore,[17,g] M. Fiorini,[17,g] M. Firlej,[28] C. Fitzpatrick,[41] T. Fiutowski,[28] F. Fleuret,[7,b] K. Fohl,[40] M. Fontana,[16,40] F. Fontanelli,[20,h] D. C. Forshaw,[61] R. Forty,[40] V. Franco Lima,[54] M. Frank,[40] C. Frei,[40] J. Fu,[22,q] W. Funk,[40] E. Furfaro,[25,j] C. Färber,[40] E. Gabriel,[52] A. Gallas Torreira,[39] D. Galli,[15,e] S. Gallorini,[23] S. Gambetta,[52] M. Gandelman,[2] P. Gandini,[57] Y. Gao,[3] L. M. Garcia Martin,[70] J. García Pardiñas,[39] J. Garra Tico,[49] L. Garrido,[38] P. J. Garsed,[49] D. Gascon,[38] C. Gaspar,[40] L. Gavardi,[10] G. Gazzoni,[5] D. Gerick,[12] E. Gersabeck,[12] M. Gersabeck,[56] T. Gershon,[50] Ph. Ghez,[4] S. Gianì,[41] V. Gibson,[49] O. G. Girard,[41] L. Giubega,[30] K. Gizdov,[52] V. V. Gligorov,[8] D. Golubkov,[32] A. Golutvin,[55,40] A. Gomes,[1,a] I. V. Gorelov,[33] C. Gotti,[21,i] E. Govorkova,[43] J. P. Grabowski,[12] R. Graciani Diaz,[38] L. A. Granado Cardoso,[40] E. Graugés,[38] E. Graverini,[42] G. Graziani,[18] A. Grecu,[30] R. Greim,[9] P. Griffith,[16] L. Grillo,[21,40,i] L. Gruber,[40] B. R. Gruberg Cazon,[57] O. Grünberg,[67] E. Gushchin,[34] Yu. Guz,[37] T. Gys,[40] C. Göbel,[62] T. Hadavizadeh,[57] C. Hadjivasiliou,[5] G. Haefeli,[41] C. Haen,[40] S. C. Haines,[49] B. Hamilton,[60] X. Han,[12] T. H. Hancock,[57] S. Hansmann-Menzemer,[12] N. Harnew,[57] S. T. Harnew,[48] J. Harrison,[56] C. Hasse,[40] M. Hatch,[40] J. He,[63] M. Hecker,[55] K. Heinicke,[10] A. Heister,[9] K. Hennessy,[54] P. Henrard,[5] L. Henry,[70] E. van Herwijnen,[40] M. Heß,[67] A. Hicheur,[2] D. Hill,[57] C. Hombach,[56] P. H. Hopchev,[41] Z. C. Huard,[59] W. Hulsbergen,[43] T. Humair,[55] M. Hushchyn,[35] D. Hutchcroft,[54] P. Ibis,[10] M. Idzik,[28] P. Ilten,[58] R. Jacobsson,[40] J. Jalocha,[57] E. Jans,[43] A. Jawahery,[60] F. Jiang,[3] M. John,[57] D. Johnson,[40] C. R. Jones,[49] C. Joram,[40] B. Jost,[40] N. Jurik,[57] S. Kandybei,[45] M. Karacson,[40] J. M. Kariuki,[48] S. Karodia,[53] N. Kazeev,[35] M. Kecke,[12] M. Kelsey,[61] M. Kenzie,[49] T. Ketel,[44] E. Khairullin,[35] B. Khanji,[12] C. Khurewathanakul,[41] T. Kirn,[9] S. Klaver,[56] K. Klimaszewski,[29] T. Klimkovich,[11] S. Koliiev,[46] M. Kolpin,[12] I. Komarov,[41] R. Kopecna,[12] P. Koppenburg,[43] A. Kosmyntseva,[32] S. Kotriakhova,[31] M. Kozeiha,[5] L. Kravchuk,[34] M. Kreps,[50] P. Krokovny,[36,w] F. Kruse,[10] W. Krzemien,[29] W. Kucewicz,[27,l] M. Kucharczyk,[27] V. Kudryavtsev,[36,w] A. K. Kuonen,[41] K. Kurek,[29] T. Kvaratskheliya,[32,40] D. Lacarrere,[40] G. Lafferty,[56] A. Lai,[16] G. Lanfranchi,[19] C. Langenbruch,[9] T. Latham,[50] C. Lazzeroni,[47] R. Le Gac,[6] J. van Leerdam,[43] A. Leflat,[33,40] J. Lefrançois,[7] R. Lefèvre,[5] F. Lemaitre,[40] E. Lemos Cid,[39] O. Leroy,[6] T. Lesiak,[27] B. Leverington,[12] P.-R. Li,[63] T. Li,[3] Y. Li,[7] Z. Li,[61] T. Likhomanenko,[35,68] R. Lindner,[40] F. Lionetto,[42] X. Liu,[3] D. Loh,[50] A. Loi,[16] I. Longstaff,[53] J. H. Lopes,[2] D. Lucchesi,[23,o] M. Lucio Martinez,[39] H. Luo,[52] A. Lupato,[23] E. Luppi,[17,g] O. Lupton,[40] A. Lusiani,[24] X. Lyu,[63] F. Machefert,[7] F. Maciuc,[30] V. Macko,[41] P. Mackowiak,[10] S. Maddrell-Mander,[48] O. Maev,[31,40] K. Maguire,[56] D. Maisuzenko,[31] M. W. Majewski,[28] S. Malde,[57] A. Malinin,[68] T. Maltsev,[36,w] G. Manca,[16,f] G. Mancinelli,[6] P. Manning,[61] D. Marangotto,[22,q] J. Maratas,[5,v] J. F. Marchand,[4] U. Marconi,[15] C. Marin Benito,[38] M. Marinangeli,[41] P. Marino,[24,t] J. Marks,[12] G. Martellotti,[26] M. Martin,[6] M. Martinelli,[41] D. Martinez Santos,[39] F. Martinez Vidal,[70] D. Martins Tostes,[2] L. M. Massacrier,[7] A. Massafferri,[1] R. Matev,[40] A. Mathad,[50] Z. Mathe,[40] C. Matteuzzi,[21] A. Mauri,[42] E. Maurice,[7,b] B. Maurin,[41] A. Mazurov,[47] M. McCann,[55,40] A. McNab,[56] R. McNulty,[13] J. V. Mead,[54] B. Meadows,[59] C. Meaux,[6] F. Meier,[10] N. Meinert,[67] D. Melnychuk,[29] M. Merk,[43] A. Merli,[22,40,q] E. Michielin,[23] D. A. Milanes,[66] E. Millard,[50] M.-N. Minard,[4] L. Minzoni,[17] D. S. Mitzel,[12] A. Mogini,[8] J. Molina Rodriguez,[1] T. Mombächer,[10] I. A. Monroy,[66] S. Monteil,[5] M. Morandin,[23] M. J. Morello,[24,t] O. Morgunova,[68] J. Moron,[28] A. B. Morris,[52] R. Mountain,[61] F. Muheim,[52]

M. Mulder,[43] M. Mussini,[15] D. Müller,[56] J. Müller,[10] K. Müller,[42] V. Müller,[10] P. Naik,[48] T. Nakada,[41] R. Nandakumar,[51] A. Nandi,[57] I. Nasteva,[2] M. Needham,[52] N. Neri,[22,40] S. Neubert,[12] N. Neufeld,[40] M. Neuner,[12] T. D. Nguyen,[41] C. Nguyen-Mau,[41,n] S. Nieswand,[9] R. Niet,[10] N. Nikitin,[33] T. Nikodem,[12] A. Nogay,[68] D. P. O'Hanlon,[50] A. Oblakowska-Mucha,[28] V. Obraztsov,[37] S. Ogilvy,[19] R. Oldeman,[16,f] C. J. G. Onderwater,[71] A. Ossowska,[27] J. M. Otalora Goicochea,[2] P. Owen,[42] A. Oyanguren,[70] P. R. Pais,[41] A. Palano,[14,d] M. Palutan,[19,40] A. Papanestis,[51] M. Pappagallo,[14,d] L. L. Pappalardo,[17,g] W. Parker,[60] C. Parkes,[56] G. Passaleva,[18] A. Pastore,[14,d] M. Patel,[55] C. Patrignani,[15,e] A. Pearce,[40] A. Pellegrino,[43] G. Penso,[26] M. Pepe Altarelli,[40] S. Perazzini,[40] P. Perret,[5] L. Pescatore,[41] K. Petridis,[48] A. Petrolini,[20,h] A. Petrov,[68] M. Petruzzo,[22,q] E. Picatoste Olloqui,[38] B. Pietrzyk,[4] M. Pikies,[27] D. Pinci,[26] F. Pisani,[40] A. Pistone,[20,h] A. Piucci,[12] V. Placinta,[30] S. Playfer,[52] M. Plo Casasus,[39] F. Polci,[8] M. Poli Lener,[19] A. Poluektov,[50,36] I. Polyakov,[61] E. Polycarpo,[2] G. J. Pomery,[48] S. Ponce,[40] A. Popov,[37] D. Popov,[11,40] S. Poslavskii,[37] C. Potterat,[2] E. Price,[48] J. Prisciandaro,[39] C. Prouve,[48] V. Pugatch,[46] A. Puig Navarro,[42] H. Pullen,[57] G. Punzi,[24,p] W. Qian,[50] R. Quagliani,[7,48] B. Quintana,[5] B. Rachwal,[28] J. H. Rademacker,[48] M. Rama,[24] M. Ramos Pernas,[39] M. S. Rangel,[2] I. Raniuk,[45,†] F. Ratnikov,[35] G. Raven,[44] M. Ravonel Salzgeber,[40] M. Reboud,[4] F. Redi,[55] S. Reichert,[10] A. C. dos Reis,[1] C. Remon Alepuz,[70] V. Renaudin,[7] S. Ricciardi,[51] S. Richards,[48] M. Rihl,[40] K. Rinnert,[54] V. Rives Molina,[38] P. Robbe,[7] A. B. Rodrigues,[1] E. Rodrigues,[59] J. A. Rodriguez Lopez,[66] P. Rodriguez Perez,[56,†] A. Rogozhnikov,[35] S. Roiser,[40] A. Rollings,[57] V. Romanovskiy,[37] A. Romero Vidal,[39] J. W. Ronayne,[13] M. Rotondo,[19] M. S. Rudolph,[61] T. Ruf,[40] P. Ruiz Valls,[70] J. Ruiz Vidal,[70] J. J. Saborido Silva,[39] E. Sadykhov,[32] N. Sagidova,[31] B. Saitta,[16,f] V. Salustino Guimaraes,[1] C. Sanchez Mayordomo,[70] B. Sanmartin Sedes,[39] R. Santacesaria,[26] C. Santamarina Rios,[39] M. Santimaria,[19] E. Santovetti,[25,j] G. Sarpis,[56] A. Sarti,[26] C. Satriano,[26,s] A. Satta,[25] D. M. Saunders,[48] D. Savrina,[32,33] S. Schael,[9] M. Schellenberg,[10] M. Schiller,[53] H. Schindler,[40] M. Schlupp,[10] M. Schmelling,[11] T. Schmelzer,[10] B. Schmidt,[40] O. Schneider,[41] A. Schopper,[40] H. F. Schreiner,[59] K. Schubert,[10] M. Schubiger,[41] M.-H. Schune,[7] R. Schwemmer,[40] B. Sciascia,[19] A. Sciubba,[26,k] A. Semennikov,[32] A. Sergi,[47] N. Serra,[42] J. Serrano,[6] L. Sestini,[23] P. Seyfert,[40] M. Shapkin,[37] I. Shapoval,[45] Y. Shcheglov,[31] T. Shears,[54] L. Shekhtman,[36,w] V. Shevchenko,[68] B. G. Siddi,[17,40] R. Silva Coutinho,[42] L. Silva de Oliveira,[2] G. Simi,[23,o] S. Simone,[14,d] M. Sirendi,[49] N. Skidmore,[48] T. Skwarnicki,[61] E. Smith,[55] I. T. Smith,[52] J. Smith,[49] M. Smith,[55] l. Soares Lavra,[1] M. D. Sokoloff,[59] F. J. P. Soler,[53] B. Souza De Paula,[2] B. Spaan,[10] P. Spradlin,[53] S. Sridharan,[40] F. Stagni,[40] M. Stahl,[12] S. Stahl,[40] P. Stefko,[41] S. Stefkova,[55] O. Steinkamp,[42] S. Stemmle,[12] O. Stenyakin,[37] M. Stepanova,[31] H. Stevens,[10] S. Stone,[61] B. Storaci,[42] S. Stracka,[24,p] M. E. Stramaglia,[41] M. Straticiuc,[30] U. Straumann,[42] L. Sun,[64] W. Sutcliffe,[55] K. Swientek,[28] V. Syropoulos,[44] M. Szczekowski,[29] T. Szumlak,[28] M. Szymanski,[63] S. T'Jampens,[4] A. Tayduganov,[6] T. Tekampe,[10] G. Tellarini,[17,g] F. Teubert,[40] E. Thomas,[40] J. van Tilburg,[43] M. J. Tilley,[55] V. Tisserand,[4] M. Tobin,[41] S. Tolk,[49] L. Tomassetti,[17,g] D. Tonelli,[24] F. Toriello,[61] R. Tourinho Jadallah Aoude,[1] E. Tournefier,[4] M. Traill,[53] M. T. Tran,[41] M. Tresch,[42] A. Trisovic,[40] A. Tsaregorodtsev,[6] P. Tsopelas,[43] A. Tully,[49] N. Tuning,[43,40] A. Ukleja,[29] A. Ustyuzhanin,[35] U. Uwer,[12] C. Vacca,[16,f] A. Vagner,[69] V. Vagnoni,[15,40] A. Valassi,[40] S. Valat,[40] G. Valenti,[15] R. Vazquez Gomez,[19] P. Vazquez Regueiro,[39] S. Vecchi,[17] M. van Veghel,[43] J. J. Velthuis,[48] M. Veltri,[18,r] G. Veneziano,[57] A. Venkateswaran,[61] T. A. Verlage,[9] M. Vernet,[5] M. Vesterinen,[57] J. V. Viana Barbosa,[40] B. Viaud,[7] D. Vieira,[63] M. Vieites Diaz,[39] H. Viemann,[67] X. Vilasis-Cardona,[38,m] M. Vitti,[49] V. Volkov,[33] A. Vollhardt,[42] B. Voneki,[40] A. Vorobyev,[31] V. Vorobyev,[36,w] C. Voß,[9] J. A. de Vries,[43] C. Vázquez Sierra,[39] R. Waldi,[67] C. Wallace,[50] R. Wallace,[13] J. Walsh,[24] J. Wang,[61] D. R. Ward,[49] H. M. Wark,[54] N. K. Watson,[47] D. Websdale,[55] A. Weiden,[42] M. Whitehead,[40] J. Wicht,[50] G. Wilkinson,[57,40] M. Wilkinson,[61] M. Williams,[56] M. P. Williams,[47] M. Williams,[58] T. Williams,[47] F. F. Wilson,[51] J. Wimberley,[60] M. Winn,[7] J. Wishahi,[10] W. Wislicki,[29] M. Witek,[27] G. Wormser,[7] S. A. Wotton,[49] K. Wraight,[53] K. Wyllie,[40] Y. Xie,[65] Z. Xu,[4] Z. Yang,[3] Z. Yang,[60] Y. Yao,[61] H. Yin,[65] J. Yu,[65] X. Yuan,[61] O. Yushchenko,[37] K. A. Zarebski,[47] M. Zavertyaev,[11,c] L. Zhang,[3] Y. Zhang,[7] A. Zhelezov,[12] Y. Zheng,[63] X. Zhu,[3] V. Zhukov,[33] J. B. Zonneveld,[52] and S. Zucchelli[15]

(LHCb Collaboration)

[1]*Centro Brasileiro de Pesquisas Físicas (CBPF), Rio de Janeiro, Brazil*
[2]*Universidade Federal do Rio de Janeiro (UFRJ), Rio de Janeiro, Brazil*
[3]*Center for High Energy Physics, Tsinghua University, Beijing, China*
[4]*LAPP, Université Savoie Mont-Blanc, CNRS/IN2P3, Annecy-Le-Vieux, France*
[5]*Clermont Université, Université Blaise Pascal, CNRS/IN2P3, LPC, Clermont-Ferrand, France*

[6]Aix Marseille Univ, CNRS/IN2P3, CPPM, Marseille, France
[7]LAL, Univ. Paris-Sud, CNRS/IN2P3, Université Paris-Saclay, Orsay, France
[8]LPNHE, Université Pierre et Marie Curie, Université Paris Diderot, CNRS/IN2P3, Paris, France
[9]I. Physikalisches Institut, RWTH Aachen University, Aachen, Germany
[10]Fakultät Physik, Technische Universität Dortmund, Dortmund, Germany
[11]Max-Planck-Institut für Kernphysik (MPIK), Heidelberg, Germany
[12]Physikalisches Institut, Ruprecht-Karls-Universität Heidelberg, Heidelberg, Germany
[13]School of Physics, University College Dublin, Dublin, Ireland
[14]Sezione INFN di Bari, Bari, Italy
[15]Sezione INFN di Bologna, Bologna, Italy
[16]Sezione INFN di Cagliari, Cagliari, Italy
[17]Universita e INFN, Ferrara, Ferrara, Italy
[18]Sezione INFN di Firenze, Firenze, Italy
[19]Laboratori Nazionali dell'INFN di Frascati, Frascati, Italy
[20]Sezione INFN di Genova, Genova, Italy
[21]Universita & INFN, Milano-Bicocca, Milano, Italy
[22]Sezione di Milano, Milano, Italy
[23]Sezione INFN di Padova, Padova, Italy
[24]Sezione INFN di Pisa, Pisa, Italy
[25]Sezione INFN di Roma Tor Vergata, Roma, Italy
[26]Sezione INFN di Roma La Sapienza, Roma, Italy
[27]Henryk Niewodniczanski Institute of Nuclear Physics Polish Academy of Sciences, Kraków, Poland
[28]AGH - University of Science and Technology, Faculty of Physics and Applied Computer Science, Kraków, Poland
[29]National Center for Nuclear Research (NCBJ), Warsaw, Poland
[30]Horia Hulubei National Institute of Physics and Nuclear Engineering, Bucharest-Magurele, Romania
[31]Petersburg Nuclear Physics Institute (PNPI), Gatchina, Russia
[32]Institute of Theoretical and Experimental Physics (ITEP), Moscow, Russia
[33]Institute of Nuclear Physics, Moscow State University (SINP MSU), Moscow, Russia
[34]Institute for Nuclear Research of the Russian Academy of Sciences (INR RAN), Moscow, Russia
[35]Yandex School of Data Analysis, Moscow, Russia
[36]Budker Institute of Nuclear Physics (SB RAS), Novosibirsk, Russia
[37]Institute for High Energy Physics (IHEP), Protvino, Russia
[38]ICCUB, Universitat de Barcelona, Barcelona, Spain
[39]Universidad de Santiago de Compostela, Santiago de Compostela, Spain
[40]European Organization for Nuclear Research (CERN), Geneva, Switzerland
[41]Institute of Physics, Ecole Polytechnique Fédérale de Lausanne (EPFL), Lausanne, Switzerland
[42]Physik-Institut, Universität Zürich, Zürich, Switzerland
[43]Nikhef National Institute for Subatomic Physics, Amsterdam, The Netherlands
[44]Nikhef National Institute for Subatomic Physics and VU University Amsterdam, Amsterdam, The Netherlands
[45]NSC Kharkiv Institute of Physics and Technology (NSC KIPT), Kharkiv, Ukraine
[46]Institute for Nuclear Research of the National Academy of Sciences (KINR), Kyiv, Ukraine
[47]University of Birmingham, Birmingham, United Kingdom
[48]H.H. Wills Physics Laboratory, University of Bristol, Bristol, United Kingdom
[49]Cavendish Laboratory, University of Cambridge, Cambridge, United Kingdom
[50]Department of Physics, University of Warwick, Coventry, United Kingdom
[51]STFC Rutherford Appleton Laboratory, Didcot, United Kingdom
[52]School of Physics and Astronomy, University of Edinburgh, Edinburgh, United Kingdom
[53]School of Physics and Astronomy, University of Glasgow, Glasgow, United Kingdom
[54]Oliver Lodge Laboratory, University of Liverpool, Liverpool, United Kingdom
[55]Imperial College London, London, United Kingdom
[56]School of Physics and Astronomy, University of Manchester, Manchester, United Kingdom
[57]Department of Physics, University of Oxford, Oxford, United Kingdom
[58]Massachusetts Institute of Technology, Cambridge, Massachusetts, USA
[59]University of Cincinnati, Cincinnati, Ohio, USA
[60]University of Maryland, College Park, Maryland, USA
[61]Syracuse University, Syracuse, New York, USA
[62]Pontifícia Universidade Católica do Rio de Janeiro (PUC-Rio), Rio de Janeiro, Brazil, [associated with Universidade Federal do Rio de Janeiro (UFRJ), Rio de Janeiro, Brazil]

[63]*University of Chinese Academy of Sciences, Beijing, China, (associated with Center for High Energy Physics, Tsinghua University, Beijing, China)*
[64]*School of Physics and Technology, Wuhan University, Wuhan, China, (associated with Center for High Energy Physics, Tsinghua University, Beijing, China)*
[65]*Institute of Particle Physics, Central China Normal University, Wuhan, Hubei, China, (associated with Center for High Energy Physics, Tsinghua University, Beijing, China)*
[66]*Departamento de Fisica, Universidad Nacional de Colombia, Bogota, Colombia, (associated with LPNHE, Université Pierre et Marie Curie, Université Paris Diderot, CNRS/IN2P3, Paris, France)*
[67]*Institut für Physik, Universität Rostock, Rostock, Germany, (associated with Physikalisches Institut, Ruprecht-Karls-Universität Heidelberg, Heidelberg, Germany)*
[68]*National Research Centre Kurchatov Institute, Moscow, Russia, [associated with Institute of Theoretical and Experimental Physics (ITEP), Moscow, Russia]*
[69]*National Research Tomsk Polytechnic University, Tomsk, Russia, [associated with Institute of Theoretical and Experimental Physics (ITEP), Moscow, Russia]*
[70]*Instituto de Fisica Corpuscular, Centro Mixto Universidad de Valencia - CSIC, Valencia, Spain, (associated with ICCUB, Universitat de Barcelona, Barcelona, Spain)*
[71]*Van Swinderen Institute, University of Groningen, Groningen, The Netherlands, (associated with Nikhef National Institute for Subatomic Physics, Amsterdam, The Netherlands)*

[†]Deceased.
[a]Also at Universidade Federal do Triângulo Mineiro (UFTM), Uberaba-MG, Brazil.
[b]Also at Laboratoire Leprince-Ringuet, Palaiseau, France.
[c]Also at P.N. Lebedev Physical Institute, Russian Academy of Science (LPI RAS), Moscow, Russia.
[d]Also at Università di Bari, Bari, Italy.
[e]Also at Università di Bologna, Bologna, Italy.
[f]Also at Università di Cagliari, Cagliari, Italy.
[g]Also at Università di Ferrara, Ferrara, Italy.
[h]Also at Università di Genova, Genova, Italy.
[i]Also at Università di Milano Bicocca, Milano, Italy.
[j]Also at Università di Roma Tor Vergata, Roma, Italy.
[k]Also at Università di Roma La Sapienza, Roma, Italy.
[l]Also at AGH - University of Science and Technology, Faculty of Computer Science, Electronics and Telecommunications, Kraków, Poland.
[m]Also at LIFAELS, La Salle, Universitat Ramon Llull, Barcelona, Spain.
[n]Also at Hanoi University of Science, Hanoi, Viet Nam.
[o]Also at Università di Padova, Padova, Italy.
[p]Also at Università di Pisa, Pisa, Italy.
[q]Also at Università degli Studi di Milano, Milano, Italy.
[r]Also at Università di Urbino, Urbino, Italy.
[s]Also at Università della Basilicata, Potenza, Italy.
[t]Also at Scuola Normale Superiore, Pisa, Italy.
[u]Also at Università di Modena e Reggio Emilia, Modena, Italy.
[v]Also at Iligan Institute of Technology (IIT), Iligan, Philippines.
[w]Also at Novosibirsk State University, Novosibirsk, Russia.